



**HAL**  
open science

# Structure, stress, and mechanical properties of Mo-Al-N thin films deposited by dc reactive magnetron cosputtering: Role of point defects

Firat Anğay, Lukas Löfler, Florent Tetard, Dominique Eyidi, Philippe Djemia, David Holec, Gregory Abadias

## ► To cite this version:

Firat Anğay, Lukas Löfler, Florent Tetard, Dominique Eyidi, Philippe Djemia, et al.. Structure, stress, and mechanical properties of Mo-Al-N thin films deposited by dc reactive magnetron cosputtering: Role of point defects. *Journal of Vacuum Science & Technology A*, 2020, 38 (5), pp.053401. 10.1116/6.0000292 . hal-03036835

**HAL Id: hal-03036835**

**<https://hal.science/hal-03036835v1>**

Submitted on 2 Dec 2020

**HAL** is a multi-disciplinary open access archive for the deposit and dissemination of scientific research documents, whether they are published or not. The documents may come from teaching and research institutions in France or abroad, or from public or private research centers.

L'archive ouverte pluridisciplinaire **HAL**, est destinée au dépôt et à la diffusion de documents scientifiques de niveau recherche, publiés ou non, émanant des établissements d'enseignement et de recherche français ou étrangers, des laboratoires publics ou privés.

# Structure, stress, and mechanical properties of Mo-Al-N thin films deposited by dc reactive magnetron cosputtering: Role of point defects


Cite as: J. Vac. Sci. Technol. A **38**, 053401 (2020); <https://doi.org/10.1116/6.0000292>

Submitted: 03 May 2020 . Accepted: 19 June 2020 . Published Online: 10 July 2020

Firat Anğay<sup>1</sup>, Lukas Löfler, Florent Tetard , Dominique Eyidi, Philippe Djemia , David Holec, and Gregory Abadias 

## COLLECTIONS

Note: This paper is part of the 2020 Special Topic Collection Festschrift Honoring Dr. Steve Rossnagel.

 This paper was selected as Featured



View Online



Export Citation



CrossMark

**HIDEN**  
ANALYTICAL

## Instruments for Advanced Science

Contact Hiden Analytical for further details:

**W** [www.HidenAnalytical.com](http://www.HidenAnalytical.com)

**E** [info@hiden.co.uk](mailto:info@hiden.co.uk)

**CLICK TO VIEW** our product catalogue



### Gas Analysis

- dynamic measurement of reaction gas streams
- catalysis and thermal analysis
- molecular beam studies
- dissolved species probes
- fermentation, environmental and ecological studies



### Surface Science

- UHV/TPO
- SIMS
- end point detection in ion beam etch
- elemental imaging - surface mapping



### Plasma Diagnostics

- plasma source characterization
- etch and deposition process reaction kinetic studies
- analysis of neutral and radical species



### Vacuum Analysis

- partial pressure measurement and control of process gases
- reactive sputter process control
- vacuum diagnostics
- vacuum coating process monitoring



# Structure, stress, and mechanical properties of Mo-Al-N thin films deposited by dc reactive magnetron cosputtering: Role of point defects

Cite as: J. Vac. Sci. Technol. A 38, 053401 (2020); doi: 10.1116/6.0000292

Submitted: 3 May 2020 · Accepted: 19 June 2020 ·

Published Online: 10 July 2020



View Online



Export Citation



CrossMark

Firat Ançay,<sup>1</sup> Lukas Löfler,<sup>2</sup> Florent Tetard,<sup>3</sup>  Dominique Eyidi,<sup>1</sup> Philippe Djemia,<sup>3</sup>  David Holec,<sup>2</sup> and Gregory Abadias<sup>1,a)</sup> 

## AFFILIATIONS

<sup>1</sup>Institut Pprime, UPR 3346, CNRS-Université de Poitiers-ENSMA, 11 Boulevard Marie et Pierre Curie, TSA 41123, 86073 Poitiers Cedex 9, France

<sup>2</sup>Department of Materials Science, Montanuniversität Leoben, Franz-Josef-Strasse 18, Leoben A-8700, Austria

<sup>3</sup>Laboratoire des Sciences des Procédés et des Matériaux, UPR 3407 CNRS, Université Sorbonne Paris Nord, Alliance Sorbonne Paris Cité, 99 Avenue J.B. Clément, 93430 Villeteuse, France

**Note:** This paper is part of the 2020 Special Topic Collection Festschrift Honoring Dr. Steve Rossnagel.

**a) Author to whom correspondence should be addressed:** [gregory.abadias@univ-poitiers.fr](mailto:gregory.abadias@univ-poitiers.fr)

## ABSTRACT

In this work, the structural and mechanical properties of ternary Mo-Al-N alloys are investigated by combining thin film growth experiments and density functional theory (DFT) calculations.  $\text{Mo}_{1-x}\text{Al}_x\text{N}_y$  thin films ( $\sim 300$  nm thick), with various Al fractions ranging from  $x = 0$  to 0.5 and nitrogen-to-metal (Al + Mo) ratio ranging from  $y = 0.78$  to 1.38, were deposited by direct-current reactive magnetron cosputtering technique from elemental Mo and Al targets under Ar +  $\text{N}_2$  plasma discharges. The Al content was varied by changing the respective Mo and Al target powers, at a fixed  $\text{N}_2$  (20 SCCM) and Ar (25 SCCM) flow rate, and using two different substrate temperatures  $T_s = 350$  and  $500$  °C. The elemental composition, mass density, crystal structure, residual stress state, and intrinsic (growth) stress were examined by wavelength dispersive x-ray spectroscopy, x-ray reflectivity, x-ray diffraction, including pole figure and  $\sin^2 \psi$  measurements, and real-time *in situ* wafer curvature. Nanoindentation tests were carried out to determine film hardness  $H$  and elastic modulus  $E_{IT}$ , while the shear elastic constant  $C_{44}$  was measured selectively by surface Brillouin light spectroscopy. All deposited  $\text{Mo}_{1-x}\text{Al}_x\text{N}_y$  films have a cubic rock-salt crystal structure and exhibit a fiber-texture with a [001] preferred orientation. The incorporation of Al is accompanied by a rise in nitrogen content from 44 to 58 at.%, resulting in a significant increase (2%) in the lattice parameter when  $x$  increases from 0 to 0.27. This trend is opposite to what DFT calculations predict for cubic defect-free stoichiometric  $\text{Mo}_{1-x}\text{Al}_x\text{N}$  compounds and is attributed to variation in point defect concentration (nitrogen and metal vacancies) when Al substitutes for Mo. Increasing  $T_s$  from 350 to 500 °C has a minimal effect on the structural properties and phase composition of the ternary alloys but concurs to an appreciable reduction of the compressive stress from  $-5$  to  $-4$  GPa. A continuous increase and decrease in transverse sound velocity and mass density, respectively, lead to a moderate stiffening of the shear elastic constant from 130 to 144 GPa with increasing Al fraction up to  $x = 0.50$ , and a complex and nonmonotonous variation of  $H$  and  $E_{IT}$  is observed. The maximum hardness of  $\sim 33$  GPa is found for the  $\text{Mo}_{0.81}\text{Al}_{0.19}\text{N}_{1.13}$  film, with nitrogen content close to the stoichiometric composition. The experimental findings are explained based on structural and elastic constant values computed from DFT for defect-free and metal- or nitrogen-deficient rock-salt MoAlN compounds.

Published under license by AVS. <https://doi.org/10.1116/6.0000292>

## I. INTRODUCTION

Transition metal nitride (TMN) ceramic compounds have been extensively studied and applied as protective hard coatings for cutting, machining, or drilling processes as they combine refractory character, mechanical stiffness, and wear-resistance. The most widely studied TMN is TiN,<sup>1</sup> which crystallizes in the cubic B1 structure (rock-salt prototype, space group  $Fm\bar{3}m$ ). Besides its high hardness ( $\sim 25$  GPa) and chemical inertness, it is also a good optical and electronic conductor, making it attractive for decorative applications and local heating plasmonics.<sup>2–5</sup> In the past decades, efforts have been deployed to explore new ternary or multinary TMNs exhibiting superior physical and mechanical properties, such as increased thermal stability,<sup>6</sup> improved oxidation resistance,<sup>7</sup> or enhanced ductility.<sup>8–10</sup>

Molybdenum nitride (MoN) is comparatively less studied than other TMNs belonging to groups 4 (TiN, ZrN, and HfN) and 5 (VN, NbN, and TaN).<sup>3,11</sup> This is primarily because the stoichiometric MoN compound with B1 structure is mechanically and dynamically unstable.<sup>12–15</sup> However, compared to inherently brittle TiN or ZrN, MoN<sub>x</sub> compounds exhibit higher ductility. It has been predicted theoretically,<sup>8,10</sup> as well as demonstrated experimentally,<sup>9,16</sup> that TMNs alloyed with Mo manifest a more ductile character, as a result of shear elastic softening, while preserving high strength. This improved toughness is contributed to an increased valence electron concentration, due to the higher electronic population of  $4d$ -metal orbitals.<sup>10,11,17</sup>

The bulk phase diagram of the Mo-N system exhibits a rich variety of phases,<sup>18</sup> which complicates even more the assessment of phase formation in thin film form, due to the different ranges of processing parameters and physical vapor deposition techniques used for their synthesis.<sup>19</sup> This has stimulated some recent investigations aiming at determining the phase stability under different deposition conditions, as well as understanding the influence of point defects (metal and nitrogen vacancies) at the origin of stabilization of cubic MoN<sub>x</sub> compounds with off-stoichiometry.<sup>20–26</sup> The optical properties of an epitaxial cubic MoN<sub>x</sub> film ( $x = 0.69$ ) are also very appealing for ultraviolet technologies, as this compound exhibits negative and near-zero real permittivity combined with room temperature resistivity as low as  $250 \mu\Omega \text{ cm}$ .<sup>27</sup> The presence of nitrogen vacancies in MoN<sub>x</sub> is believed to impart its unique optical performance. MoN is also a suitable coating candidate to enhance the tribological properties over common hard coatings due to its low friction coefficient and reduced wear rate at temperatures lower than  $500^\circ\text{C}$ .<sup>28,29</sup>

Similarly to what has been reported for Ti-Al-N and Cr-Al-N systems, incorporation of Al into MoN is anticipated to be beneficial in terms of oxidation resistance and mechanical properties. Indeed, the major limitation of MoN coatings is the deterioration of their tribo-oxidation properties at elevated temperatures<sup>28</sup> due to the preferential formation of volatile molybdenum oxides. From powder metallurgy, no ternary MoAlN alloys could be synthesized, and it was concluded that AlN is not miscible with Mo under thermodynamic equilibrium.<sup>30</sup> However, the high quenching rate of physical vapor deposition techniques makes it possible to stabilize Mo<sub>1-x</sub>Al<sub>x</sub>N<sub>y</sub> solid solutions with extended solubility. Klimashin *et al.*<sup>31</sup> have shown that (1) the incorporation of Al stabilizes the cubic phase in the Mo-Al-N thin films up to AlN fraction of

$x = 0.57$ , and (2) a wurtzite phase is formed at higher AlN content, accompanied by a sharp decrease in the mechanical properties (hardness  $H$  and elastic modulus  $E$ ) above the crystalline transition. Despite a limited number of research studies dedicated to Mo-Al-N coatings,<sup>32–34</sup> there exists a large discrepancy in their reported mechanical properties: Yang *et al.*<sup>34</sup> observed an almost linear decrease in hardness with incorporation of Al, from  $\sim 30$  GPa at  $x = 0$  to less than 20 GPa at  $x = 0.33$ ; Xu *et al.*<sup>33</sup> reported an even greater deterioration of hardness from 28.9 GPa at  $x = 0$  to 12.3 GPa at  $x = 0.35$ , while hardening was reported by Klimashin *et al.*<sup>31</sup> in the composition range of  $x = 0.20$ – $0.55$  corresponding to a hardness plateau of  $\sim 37$  GPa. A similar scattering is found for the elastic modulus, with values spanning, for example, from  $\sim 450$  to 223 GPa for an Al fraction of  $x = 0.35$ . Although these coatings were all stabilized in a cubic structure, they exhibited different nitrogen contents, suggesting that the defect concentration at the nitrogen and metal sublattices plays a significant role on the mechanical behavior of the Mo-Al-N system.

The aim of the present study is to gain a better understanding on phase formation, defect concentration, and mechanical properties when Al substitutes for Mo in Mo-Al-N coatings. Our experimental approach encompasses a systematic investigation of the evolution of the lattice constant and mass density, stress state, nanoindentation elastic modulus and hardness, as well as shear elastic constant  $C_{44}$ , when varying the Al fraction up to  $x = 0.5$ , at fixed  $N_2$  partial pressure, and at two different substrate temperatures ( $T_s = 350$  and  $500^\circ\text{C}$ ). A rather surprising evolution of the lattice parameter versus Al fraction is observed, that is intimately related to an Al gettering effect on nitrogen incorporation into the film. Density functional theory (DFT) calculations on cubic Mo<sub>1-x</sub>Al<sub>x</sub>N<sub>y</sub> alloys considering both metal and nitrogen vacancies are employed to provide insights into the role of point defect on the structural and mechanical properties of these alloys and explain the experimental findings.

## II. EXPERIMENTAL PROCEDURE AND COMPUTATIONAL APPROACH

### A. Thin film deposition

Mo-Al-N ternary alloys were deposited on (001) Si substrates using direct current (dc) reactive magnetron cosputtering from two individual 3" planar targets in a high-vacuum (base pressure better than  $10^{-5}$  Pa) chamber designed by Alliance Concept. Two film series were investigated, corresponding to deposition at different substrate temperatures,  $T_s = 350$  and  $500^\circ\text{C}$ , respectively. Mo (99.95% purity) and Al (99.99% purity) targets were placed in a confocal configuration inside the chamber, located at 18 cm from the substrate holder and making an angle of  $25^\circ$  with respect to the substrate normal. The detailed information about the deposition chamber can be found in Ref. 35. Prior to each deposition, the Mo and Al targets were sputter-cleaned for 3 min under pure Ar plasma discharge to remove any possible surface oxides and contaminants before starting deposition.

Mo-Al-N ternary alloys were sputter-deposited in a mixture of Ar +  $N_2$  gases. Mass flow controllers were used to introduce the gases into the chamber, and the  $N_2$  partial pressure was measured by a quadruple mass spectrometer (MKS Micro Vision Plus). Ar and  $N_2$  gas flows were fixed at 25 and 20 SCCM, respectively, and

the working (total) and N<sub>2</sub> partial pressure were 0.3 and 0.15 Pa, respectively. The substrate (without any prior chemical etching) was fixed to a rotatable and heated substrate holder, which was electrically insulated from the grounded chamber. The substrate holder was rotated at 10 rpm throughout deposition to obtain homogeneous films, except for *in situ* monitoring of stress evolution (see below).

To vary the Al content in the films, cosputter deposition was performed by varying the respective Mo and Al target powers, from 100 to 300 W for Mo and from 0 to 300 W for Al, see Table I. The magnetrons were operating in an unbalanced mode (magnetically unbalanced magnetron). A radio frequency power supply (4 W) was used to bias the substrate, resulting in a dc voltage of -60 V with respect to ground potential. Deposition time was adjusted between 30 and 42 min depending on the deposition rate, so as to obtain a comparable film thickness of approximately 300 nm. Unless otherwise specified, the samples will be denoted as Mo<sub>1-x</sub>Al<sub>x</sub>N<sub>y</sub>, where x represents the Al fraction in the metal (Me) sublattice and y is the nitrogen-to-metal (N/Me) ratio.

## B. Characterization techniques

The elemental composition of the Mo<sub>1-x</sub>Al<sub>x</sub>N<sub>y</sub> films was determined by wavelength dispersive x-ray spectroscopy (WDS) using a field emission gun JEOL 7001F-TTLS scanning electron microscope (SEM) equipped with a WDS spectrometer unit from Oxford Instruments. WDS measurements were carried out at 7 kV, 7 nA, and ×10,000 magnification conditions. Prior to the measurements, WDS instrument was calibrated with Mo and AlN standards for quantification of Mo, Al, and N elements using the INCA wave software with an accuracy better than 0.5 at. %.

The mass density (ρ) of as-deposited Mo<sub>1-x</sub>Al<sub>x</sub>N<sub>y</sub> films was derived from x-ray reflectometry (XRR) measurements. XRR scans were acquired using a Seifert XRD 3000 diffractometer with a line

focus Cu source, a channel cut Ge (220) monochromator, and a scintillation detector with a resolution slit of 0.02°. The film thickness and mass density were calculated from XRR scans obtained on a thinner film series (50–100 nm), deposited under exactly the same conditions, serving as reference samples. A refinement procedure and an optical model based on Parratt formalism<sup>36</sup> were used to fit the XRR scans. Deposition rates were cross-checked for thicker films using film thickness values obtained from cross-sectional SEM images obtained at 25 kV, see Table I.

The crystalline structure and crystallographic phase identification of the as-deposited films were analyzed by x-ray diffraction (XRD) using a Seifert Space XRD TS-4 diffractometer operating in the Bragg-Brentano configuration at 30 kV and 30 mA, with a monochromatic Cu Kα wavelength (λ = 1.5418 Å) radiation and a Meteor0D detector. The XRD patterns were collected for 2θ angles ranging from 20° to 52°. The crystallite size and microstrain were derived from the XRD line profile using the single line analysis procedure proposed by de Keijser *et al.*<sup>37</sup>

The quantitative analysis of elastic strains in as-deposited Mo<sub>1-x</sub>Al<sub>x</sub>N<sub>y</sub> films was performed by employing XRD sin<sup>2</sup>ψ method using the same four-circle Seifert diffractometer. Since the films were highly textured, the so-called crystallite group method (CGM) was applied,<sup>38–40</sup> which consists in measuring multiple *hkl* reflections at several (ψ, φ) tilt and rotation angles, respectively. Note that φ was held constant here because of the fiber-texture of the films (checked using XRD pole figure measurements). From the recorded 2θ peak positions, the lattice parameter (a<sub>ψ</sub>) can be calculated for each ψ angle. Using the linear elasticity theory and single-crystal elastic constants (C<sub>11</sub>, C<sub>12</sub>, and C<sub>44</sub>) computed from DFT for cubic Mo<sub>2</sub>N and MoAlN compounds, the stress-free lattice parameter (a<sub>0</sub>) and in-plane residual stress σ (assuming a biaxial stress state) could be determined.

Besides the determination of residual stress from the XRD analysis, the evolution of intrinsic (growth) stress was monitored *in*

**TABLE I.** Process parameters for magnetron sputter-deposition of Mo<sub>1-x</sub>Al<sub>x</sub>N<sub>y</sub> films, as well as chemical and microstructural properties obtained from XRR, XRD, WDS, and SEM analyses.

Sample	Mo power (W)	Al power (W)	Substrate temperature (°C)	Elemental composition (at. %)	Al fraction (x)	N/Me ratio (y)	Film thickness (nm)	Crystallite size (nm)
MoN <sub>0.79</sub>	300	0	350	Mo <sub>56</sub> N <sub>44</sub>	0	0.79	473	—
Mo <sub>0.98</sub> Al <sub>0.02</sub> N <sub>0.92</sub>	300	50	350	Mo <sub>51</sub> Al <sub>1</sub> N <sub>48</sub>	0.02	0.92	270	280
Mo <sub>0.94</sub> Al <sub>0.06</sub> N <sub>0.92</sub>	300	100	350	Mo <sub>49</sub> Al <sub>3</sub> N <sub>48</sub>	0.06	0.92	313	—
Mo <sub>0.88</sub> Al <sub>0.12</sub> N <sub>1.08</sub>	300	200	350	Mo <sub>42</sub> Al <sub>6</sub> N <sub>52</sub>	0.12	1.08	349	340
Mo <sub>0.81</sub> Al <sub>0.19</sub> N <sub>1.13</sub>	300	300	350	Mo <sub>38</sub> Al <sub>9</sub> N <sub>53</sub>	0.19	1.13	380	378
Mo <sub>0.73</sub> Al <sub>0.27</sub> N <sub>1.22</sub>	200	300	350	Mo <sub>33</sub> Al <sub>12</sub> N <sub>55</sub>	0.27	1.22	280	290
Mo <sub>0.50</sub> Al <sub>0.50</sub> N <sub>1.38</sub>	100	300	350	Mo <sub>21</sub> Al <sub>21</sub> N <sub>58</sub>	0.50	1.38	255	235
MoN <sub>0.75</sub>	300	0	500	Mo <sub>57</sub> N <sub>43</sub>	0	0.75	473	455
Mo <sub>0.98</sub> Al <sub>0.02</sub> N <sub>0.92</sub>	300	50	500	Mo <sub>51</sub> Al <sub>1</sub> N <sub>48</sub>	0.02	0.92	270	—
Mo <sub>0.94</sub> Al <sub>0.06</sub> N <sub>0.92</sub>	300	100	500	Mo <sub>49</sub> Al <sub>3</sub> N <sub>48</sub>	0.06	0.92	313	—
Mo <sub>0.85</sub> Al <sub>0.15</sub> N <sub>1.13</sub>	300	200	500	Mo <sub>40</sub> Al <sub>7</sub> N <sub>53</sub>	0.15	1.13	349	—
Mo <sub>0.83</sub> Al <sub>0.17</sub> N <sub>1.13</sub>	300	300	500	Mo <sub>39</sub> Al <sub>8</sub> N <sub>53</sub>	0.17	1.13	378	—
Mo <sub>0.73</sub> Al <sub>0.27</sub> N <sub>1.22</sub>	200	300	500	Mo <sub>33</sub> Al <sub>12</sub> N <sub>55</sub>	0.27	1.22	280	—
Mo <sub>0.51</sub> Al <sub>0.49</sub> N <sub>1.33</sub>	100	300	500	Mo <sub>22</sub> Al <sub>21</sub> N <sub>57</sub>	0.49	1.33	255	245

<sup>a</sup>Values in italics correspond to film thickness calculated from the deposition rate and deposition time.

*operando* during growth using wafer curvature technique. A multiple-beam optical stress sensor (MOSS) developed by kSA<sup>41</sup> was employed to obtain real-time information on the dynamics of stress build-up and possible relaxation during deposition.<sup>42</sup> More details on the MOSS setup can be found elsewhere.<sup>43</sup> The biaxial stress in the growing layer was calculated from the measured curvature of the Si substrate using the modified Stoney equation,<sup>44,45</sup> linking the wafer curvature  $\kappa$  to the stress thickness product  $\sigma_f \times h_f$ , according to

$$\kappa = \frac{6\sigma_f \times h_f}{Y_s h_s^2}, \quad (1)$$

where  $Y_s$  is the elastic modulus of the substrate;  $h_s$  and  $h_f$  are the thicknesses of the substrate and the film, respectively; and  $\sigma_f$  is the average stress in the film. For these measurements, a thin Si wafer (280–300  $\mu\text{m}$  thick) was employed under stationary deposition mode.

Surface Brillouin light scattering (BLS) was performed for three angles of incidence of light ( $\alpha = 60^\circ, 70^\circ,$  and  $80^\circ$ ), varying the acoustic wavelength ( $\Lambda \sim 300$  nm) of the probed surface acoustic waves (SAWs), according to

$$\Lambda = \frac{\lambda_L}{2\sin\alpha}, \quad (2)$$

where  $\lambda_L$  is the wavelength of the light source. Hence, the SAW was calculated from the measured frequency  $F_{\text{SAW}}$  according to

$$V_{\text{SAW}} = \Lambda F_{\text{SAW}}. \quad (3)$$

For opaque film materials, the main feature visible at the lowest frequency in a BLS spectrum is the Rayleigh SAW (R) followed by less intense peaks related to the Sezawa standing waves within the film thickness.<sup>46–48</sup> For films thick enough ( $\Lambda \sim h_f$ ), the velocity of the Rayleigh SAW,  $V_R$ , is mainly dependent on transverse velocity<sup>49</sup>  $V_T = (C_{44}/\rho)^{1/2}$  through the relation  $V_R = \beta V_T$ , where  $\beta \sim 0.92$  is a slightly varying function of the whole elastic constants of the film. Thus, we can selectively measure the shear elastic modulus  $G = C_{44}$  in a plane perpendicular to the film's plane. More interestingly, in the specific case of highly  $\langle 001 \rangle$ -textured polycrystalline films, this can be directly compared to the single-crystal elastic constant calculated by DFT.

The BLS spectra were obtained at room temperature after acquisition times of 2 h. The light source was a YAG solid laser with single mode of  $\lambda_L = 532$  nm. 100 mW of a naturally  $p$ -polarized light was focused on the surface of the sample and the backscattered light was analyzed by means of a Sandercock-type 3 + 3 pass tandem Fabry–Perot interferometer.<sup>50</sup>

Nanoindentation testing was performed in the continuous stiffness mode using an XP Nanoindenter (MTS, Oak Ridge, TN, USA) with a Berkovich indenter. Maximal penetration depth was 100 nm and the maximal load was 200 mN. Batches of 20 tests at random position on the sample surface were performed at a constant strain rate of  $0.05 \text{ s}^{-1}$ . We used for the analysis a fixed Poisson ratio of  $\nu = 0.35$  for each sample. This value was calculated from DFT-computed elastic constants on the  $\gamma$ - $\text{Mo}_2\text{N}$  compound<sup>26</sup> and assuming a (001) crystal orientation,  $\nu = C_{12}/(C_{11} + C_{12})$ .

Reduced elastic modulus  $E_r = (E_{\text{IT}}/(1-\nu^2))$ , Young's modulus  $E_{\text{IT}}$ , and nanohardness  $H$  were obtained by averaging the data for in-depth indenter displacements between 30 and 50 nm by using the Oliver and Pharr method.<sup>51</sup> This range is representative of the film properties only, where no significant influence of the substrate could be detected from the depth-profile curves. Depending on the Al content and vacancy concentration, values of  $\nu$  between 0.28 and 0.38 were calculated from the present DFT  $C_{ij}$  data, but the relative errors on the determination of  $H$  and  $E_{\text{IT}}$  remain small ( $-5$  to  $+2\%$ ).

### C. Computational details

The calculations were done using DFT utilizing the Vienna *Ab initio* Simulation Package. Pseudo potentials with the projector augmented wave method and generalized gradient approximation for the electronic exchange and correlation effects were used.<sup>52,53</sup> A cutoff energy of 600 eV and a  $9 \times 9 \times 9$   $k$ -point mesh were chosen. Total energy changes of  $10^{-5}$  eV and forces of 0.01 eV/Å served as convergence criteria for the calculations.

The simulated  $\text{MoAlN}$  systems were of cubic rock-salt structure. Defect-free as well as systems with 10% vacancies at either the metal ( $V_{\text{Me}}$ ) or the nitrogen ( $V_{\text{N}}$ ) sublattice, with varying Al fractions, were considered. This defect concentration was chosen so as to span as closely as possible the range of N/Me ratio observed experimentally. In addition,  $\text{Mo}_2\text{N}$  (rock-salt with ordered vacancies) and  $\text{MoAlN}$  systems with Schottky defect, Frenkel defects, and N atoms at the metal sublattice (N antisites,  $N_{\text{Me}}$ ) were also calculated, see supplementary material.<sup>72</sup> To populate the metal sublattice and distribute the vacancies randomly, the special quasi-random structure (SQS) approach was used.<sup>54</sup> The SQS cells consisted of  $2 \times 2 \times 2$  conventional cubic cells, yielding supercells with 64 atoms. This has the consequence that the concentration of a species can change only in 1.56% increments overall or 3.12% on a sublattice. In the cases of vacancies at the metal sublattice, the vacancies were distributed between the Al and Mo atoms so as to obtain the desired Al fraction,  $x$ .

The lattice constants were calculated from the resulting volumes of the fully relaxed SQS cells to average the influence the random distribution of atoms and vacancies have on the three lattice parameters. The elastic constants were calculated using the strain/stress method.<sup>55</sup> The relaxed cells were deformed, the corresponding stresses were calculated, and from Hooke's law  $\sigma = C \epsilon$ , the stiffness tensor ( $C$ ) was determined. To represent the cubic systems, the resulting  $C$  tensor was projected to cubic symmetry, following Moakher and Norris.<sup>56</sup> The polycrystalline Young's moduli were calculated from the cubic stiffness tensors applying the Voigt–Reuss homogenization as implemented in the online tool self-consistent calculations of elasticity of multiphase aggregates.<sup>57,58</sup> The elastic modulus  $E_{100}$  along the  $\langle 100 \rangle$  direction was also considered in the discussion, being given by the inverse of the compliance elastic constant  $1/S_{11}$ .

## III. EXPERIMENTAL RESULTS

### A. Elemental composition, crystal structure, and preferred orientation

The evolution of nitrogen and aluminum contents in Mo–Al–N films deposited at varying Mo and Al powers (see values

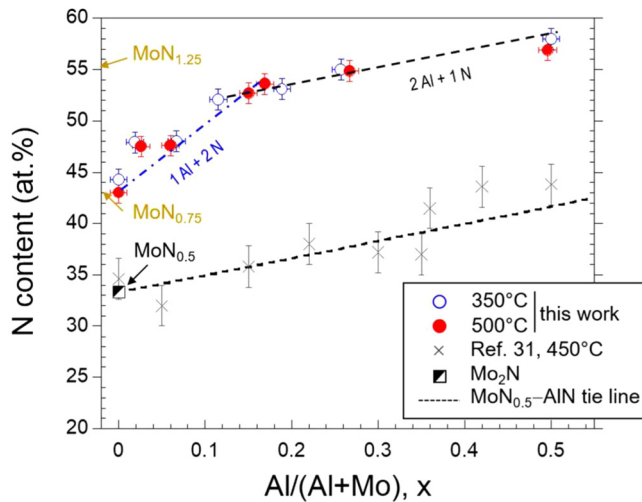


**FIG. 1.** Evolution of the nitrogen content vs Al fraction,  $x$ , for different  $\text{Mo}_{1-x}\text{Al}_x\text{N}_y$  thin films deposited at 350 °C (blue open circles) and 500 °C (red filled circles). Also shown are the data reported by Klimashin *et al.* (Ref. 31) (cross symbols) for MoAlN films sputter-deposited at 450 °C, as well as the theoretical  $\text{MoN}_{0.5}$ -AlN tie line.

in Table I) is shown in Fig. 1. It can be observed that despite the  $\text{N}_2$  flow rate being fixed at the same value of 20 SCCM for all samples, the nitrogen content evolves with the incorporation of Al in the films. Increasing the substrate temperature from 350 to 500 °C has little influence on the elemental composition but affects the lattice parameter as it will be discussed later. The binary MoN films have a composition  $\text{Mo}_{56}\text{N}_{44}$  and  $\text{Mo}_{57}\text{N}_{43}$ , i.e., the N/Me ratio  $y \sim 0.75$  lies between that of  $\text{Mo}_2\text{N}$  ( $y = 0.5$ ) and MoN ( $y = 1.0$ ). Compared to  $\gamma$ - $\text{Mo}_2\text{N}$  compound, this suggests the existence of Mo vacancies, N interstitials, N at Mo sites ( $\text{N}_{\text{Mo}}$  antisites), and/or a lower nitrogen vacancy ( $V_{\text{N}}$ ) concentration at octahedral sites. As the power of the Al target increases from 50 to 300 W, the Al content in the Mo-Al-N ternary alloy films increases from 1 to 21 at. %, with a corresponding decrease of Mo content from 56 to 21 at. %. Concurrently, the N content is found to continuously vary from 44 to 58 at. %. Therefore, the N composition evolves from substoichiometric ( $y \sim 0.75$ ) to overstoichiometric ( $y \sim 1.38$ ) with

increasing Al content, see Table I. In the study by Klimashin *et al.*<sup>31</sup> on Mo-Al-N films sputtered from a composite target at  $p_{\text{N}_2}/p_{\text{tot}} = 0.32$ , the nitrogen content increased linearly from  $\sim 33$  to 44 at. % with Al fraction increasing up to  $x = 0.5$  (see cross symbols in Fig. 1), following the  $\text{MoN}_{0.5}$ -AlN tie line (see dashed line in Fig. 1). In the present work, the nitrogen dependence on Al fraction is not linear, and two distinct regimes can be distinguished, corresponding roughly to incorporation of 2 N atoms for 1 Al atom until  $x = 0.12$  (dashed-dotted line in Fig. 1) and then 1 N atom for 2 Al atoms (dashed line) for  $0.12 \leq x \leq 0.50$ . This points out to a varying nitrogen affinity with increasing Al content. The sharp rise in nitrogen from 44 to 48 at. % upon incorporation of a minute amount of Al ( $x = 0.02$ ) advocates for an aluminum gettering effect.

As evidenced from cross-sectional SEM imaging (see Fig. 2), the Mo-Al-N films deposited at 350 °C exhibit a columnar microstructure, as typically observed in sputter-deposited TMN coatings.<sup>59</sup> The columns are found to be compact and straight, extending throughout the entire film thickness. With increasing Al content, they tend to slightly enlarge and become more clearly defined, which could traduce some tendency for competitive columnar growth. The films deposited at 500 °C have a similar microstructure, with no appreciable difference for a given Al fraction.

The evolution of the mass density versus Al content, as derived from XRR measurements, is displayed in Fig. 3. With increasing Al content, the mass density decreases from  $\rho = 9.65 \pm 0.1 \text{ g cm}^{-3}$  at  $x = 0$  to  $\rho = 6.6 \pm 0.1 \text{ g cm}^{-3}$  at  $x = 0.5$ . The Al-free films have a density that is slightly higher by 1.8% to that of the cubic  $\gamma$ - $\text{Mo}_2\text{N}$  compound ( $9.48 \text{ g cm}^{-3}$ ). The initial drop in  $\rho$  is larger upon incorporation of small Al fraction ( $x \leq 0.06$ ), but then  $\rho$  decreases almost linearly with Al fraction. The compositional dependence of the mass density of  $\text{Mo}_{1-x}\text{Al}_x\text{N}_y$  films is similar for both substrate temperatures.

The  $\theta$ - $2\theta$  XRD patterns of the  $\text{Mo}_{1-x}\text{Al}_x\text{N}_y$  films deposited at 350 °C for different Al contents are displayed in Fig. 4 (intensity in the logarithmic scale, blue line). The XRD patterns were measured along an angular  $2\theta$  range from 20° to 52° but are only shown here in the 30°–52° angular range covering the two main diffraction lines detected around 37.4° and 43.4°. The position of these lines is consistent with diffraction lines from the (111) and (200) planes of the cubic  $\gamma$ - $\text{Mo}_2\text{N}$  phase (JCPDS card No. 25-1366). XRD pole figure measurements (not shown here) confirm that the deposited Mo-Al-N ternary alloy films crystallize in a cubic structure and develop a pronounced [001] out-of-plane orientation (fiber-texture

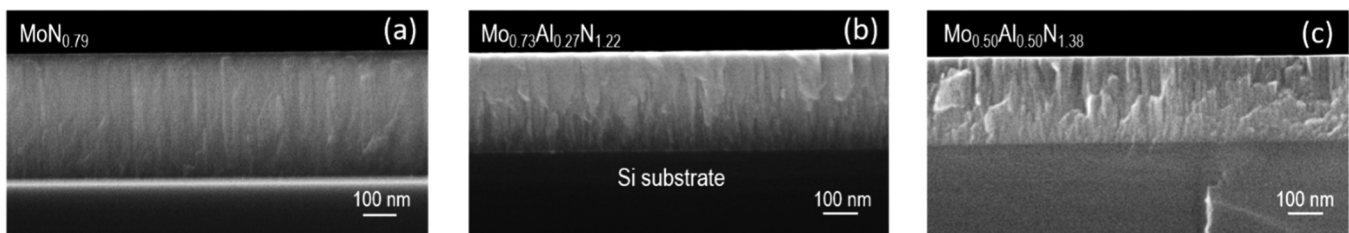


**FIG. 2.** Cross-sectional SEM micrographs of (a)  $\text{MoN}_{0.79}$ , (b)  $\text{Mo}_{0.73}\text{Al}_{0.27}\text{N}_{1.22}$ , and (c)  $\text{Mo}_{0.50}\text{Al}_{0.50}\text{N}_{1.38}$  thin films deposited at 350 °C.

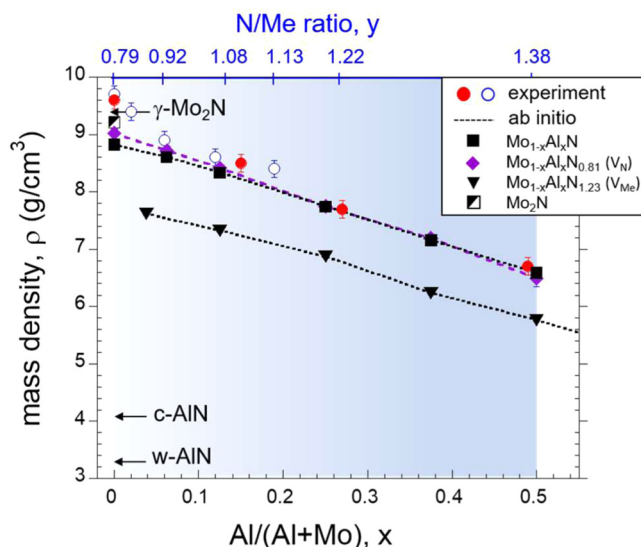


**FIG. 3.** Evolution of the mass density,  $\rho$ , of  $\text{Mo}_{1-x}\text{Al}_x\text{N}_y$  thin films with Al fraction,  $x$ , and substrate temperature  $T_s = 350^\circ\text{C}$  (blue open circles) and  $T_s = 500^\circ\text{C}$  (red filled circles). Computed DFT values for several ternary alloys with different vacancy concentrations are also shown. The upper horizontal scale giving the N/Me ratio,  $y$ , in the films (with the corresponding variation also displayed as increasing hue of the blue shaded area) is only valid for the experiments. Reference values from bulk powders are also shown with arrows for  $\gamma\text{-Mo}_2\text{N}$  (JCPDS Card No. 25-1366), stable w-AlN (JCPDS Card No. 25-1133), and metastable c-AlN (JCPDS Card No. 46-1200).

type). For all  $\text{Mo}_{1-x}\text{Al}_x\text{N}_y$  films, other reflections from either wurtzite AlN or hexagonal  $\epsilon\text{-MoN}$  phases could not be detected.

With increasing Al content, the position of the main 200 XRD line gradually shifts to lower  $2\theta$  angles, except between  $x = 0.27$  and  $x = 0.5$  for which the XRD lines move relatively from left to right. This, together with the absence of reflections from pure AlN phase, suggests the formation of  $\text{Mo}_{1-x}\text{Al}_x\text{N}_y$  solid solutions in the investigated Al range, and the existence of two distinct regimes, below and above  $x = 0.12$ , in agreement with the decreasing incorporation rate of nitrogen discussed above. The evolution of the lattice parameter with Al content will be examined in detail in Sec. III B, where the issue of residual stress is addressed. Besides this peak shift, one can notice a decrease in the 200 XRD line intensity, accompanied by an increase in the intensity of the 111 XRD line, with increasing Al content. The XRD patterns of the films deposited at  $500^\circ\text{C}$  (red lines in Fig. 4) are very similar to those obtained at  $350^\circ\text{C}$ , albeit a noticeable shift of XRD lines toward higher  $2\theta$  angles. Overall, the intensity of the 200 XRD lines is higher at  $500^\circ\text{C}$  than at  $350^\circ\text{C}$ , traducing an improvement in the (001) texture.

Note that the 200 XRD line profile for the binary  $\text{MoN}_{0.79}$  and  $\text{MoN}_{0.75}$  films appears peculiar, with a large asymmetry toward lower  $2\theta$  angles. This could be attributed to the presence of a significant fraction of point defects (of vacancy-type) such as also observed in sputtered TaN layers<sup>60</sup> or attests the presence of strain gradients. However, no diffraction lines around  $20^\circ$  could

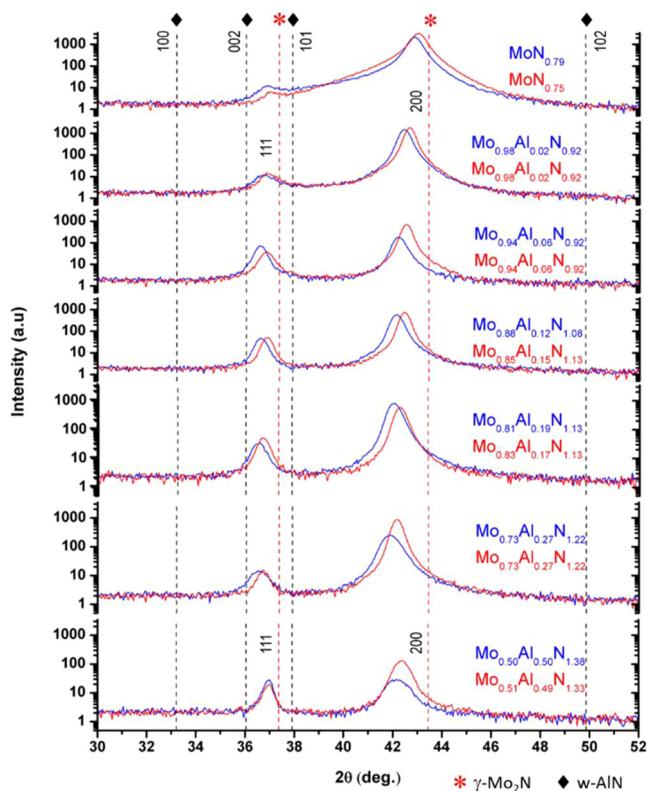


**FIG. 4.** XRD patterns of  $\text{Mo}_{1-x}\text{Al}_x\text{N}_y$  thin films deposited at  $350^\circ\text{C}$  (blue line) and  $500^\circ\text{C}$  (red line). Vertical dashed lines indicate hkl reflections of bulk w-AlN and  $\gamma\text{-Mo}_2\text{N}$  compounds.

be detected, contrarily to what has been reported by Klimashin *et al.* in sputtered MoN films<sup>20</sup> and assigned to superstructure reflection arising from a cubic  $\gamma\text{-MoN}_{0.67}$  compound (space group  $Pm\bar{3}m$ ) with ordered vacancies.<sup>61</sup> It is certainly due to the reduced nitrogen vacancy concentration in our binary films ( $\text{MoN}_{\sim 0.75}$ ) that can favor more random distribution, as also supported by DFT calculations.<sup>20</sup>

Estimation of grain size and microstrain variations with Al content was obtained from XRD line broadening using the single-line analysis method proposed by de Keijser *et al.*,<sup>37</sup> which is based on determining the Cauchy and Gaussian integral breadth of a given Bragg reflection. Grain size values determined from 200 XRD line are reported in Table I. It can be observed that the grain size varied from  $20 \pm 5$  to  $38 \pm 5$  nm for  $\text{Mo}_{1-x}\text{Al}_x\text{N}_y$  films deposited at  $350^\circ\text{C}$  and from  $15 \pm 5$  to  $66 \pm 5$  nm for films deposited at  $500^\circ\text{C}$ . The smallest grain sizes were found for the binary films. Incorporation of Al in the films up to  $x = 0.12$  leads first to an increase in grain size, followed by a grain refinement at higher Al content. Films deposited at  $500^\circ\text{C}$  exhibit overall larger grain sizes. Typical microstrain values (not reported in Table I) are in the  $3 - 6 \times 10^{-3}$  range. These values are consistent with those reported for cubic ternary TiTaN or TiZrN sputtered films.<sup>62</sup>



### B. Stress analysis: XRD residual stress and *in situ* stress evolution during growth

XRD strain-stress analysis of the as-deposited samples has been performed using CGM. Due to the strong (001) preferred orientation of the films, multiple reflections from (111), (200), and (311) planes were measured at specific  $\psi$  angles corresponding to the intensity poles of the cubic 001 pole figure.<sup>46</sup> The  $\sin^2\psi$  plots are shown in Fig. 5 for  $T_s = 350$  and  $500^\circ\text{C}$  film series. For all investigated samples, a linear dependence of the lattice parameter  $a_\psi$  with  $\sin^2\psi$  is observed. No  $\psi$ -splitting was evidenced, which means negligible shear stress components. From the sign of the slope of the  $\sin^2\psi$  lines, it can be concluded that all films are subjected to (in-plane) compressive residual stress. A qualitative inspection of the  $\sin^2\psi$  plots of  $\text{Mo}_{1-x}\text{Al}_x\text{N}_y$  films deposited at  $T_s = 350^\circ\text{C}$  [Fig. 5(a)] reveals that  $\sin^2\psi$  lines are vertically shifted for films with different elemental compositions, but there is no significant change in their slope. Similar observations can be made for the films series deposited at  $T_s = 500^\circ\text{C}$  [Fig. 5(b)], albeit the absolute magnitude of the slope is smaller. These trends suggest that the peak shift observed in the  $\theta$ - $2\theta$  XRD patterns of films with varying Al content is mainly

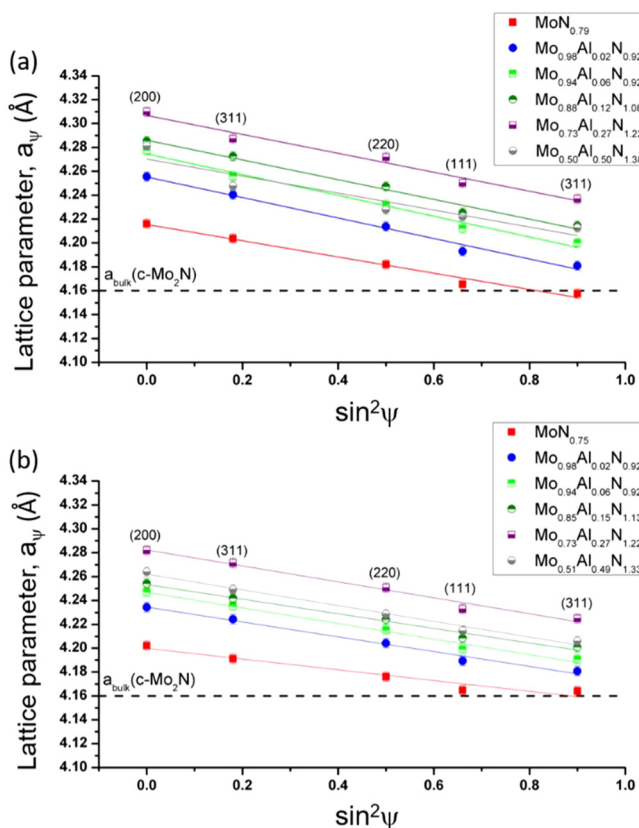


FIG. 5. Typical  $\sin^2\psi$  plots obtained on  $\text{Mo}_{1-x}\text{Al}_x\text{N}_y$  thin films deposited at  $T_s = 350^\circ\text{C}$  (a) and  $T_s = 500^\circ\text{C}$  (b).

dominated by chemical effects rather than being affected by variations in the stress state, and that the peak shift observed at  $500^\circ\text{C}$  is likely due to reduction in compressive stress.

To get quantitative estimates of the stress-free lattice parameter,  $a_0$ , and in-plane stresses, the data shown in Fig. 5 were fitted using the linear elastic theory and assuming (1) a perfect (001) texture and (2) an equibiaxial stress state  $\sigma_{11} = \sigma_{22} = \sigma$ . For  $x = 0$ , the elastic constants of the  $\gamma$ - $\text{Mo}_2\text{N}$  compound computed by DFT were used, namely,  $C_{11} = 510$  GPa,  $C_{12} = 199$  GPa, and  $C_{44} = 105$  GPa, see supplementary material.<sup>72</sup> For ternary alloys, the following set of elastic constants was chosen, taken from the  $\text{Mo}_{0.75}\text{Al}_{0.25}\text{N}$  compound, also computed by DFT:  $C_{11} = 473$  GPa,  $C_{12} = 191$  GPa, and  $C_{44} = 101$  GPa, see supplementary material.<sup>72</sup> Note that the expression of  $a_\psi$  only depends on  $C_{11}$  and  $C_{12}$  in the case of (001) texture.<sup>40</sup>

Figure 6 displays the evolution of  $\sigma$  versus Al fraction for the two film series. It can be observed that increasing the substrate temperature from  $T_s = 350$  to  $500^\circ\text{C}$  is accompanied by a reduction of the compressive stress by approximately 20%, the absolute magnitude being ranging from 4.7–5.7 to 3.3–4.4 GPa, respectively. At  $T_s = 350^\circ\text{C}$ , the variation of stress is not monotonous with Al content: a compressive stress peak is found at  $x = 0.06$  where the compressive stress level reaches  $5.7 \pm 0.3$  GPa, followed by a gradual decrease down to  $4.7 \pm 0.3$  GPa at  $x = 0.5$ . At  $T_s = 500^\circ\text{C}$ , the stress initially increases with the incorporation of a few percent of Al but then remains practically constant at 4.4 GPa for higher Al fraction.

The evolution of  $a_0$  versus Al fraction is plotted in Fig. 7 for  $\text{Mo}_{1-x}\text{Al}_x\text{N}_y$  films deposited at  $350^\circ\text{C}$  (blue symbols) and  $500^\circ\text{C}$  (red symbols). For the  $350^\circ\text{C}$  film series, one can observe that the stress-free lattice parameter first increases rapidly from  $a_0 = 4.186 \pm 0.005 \text{ \AA}$  for the binary  $\text{MoN}_{0.79}$  film to  $a_0 = 4.248 \pm 0.005 \text{ \AA}$  for the ternary

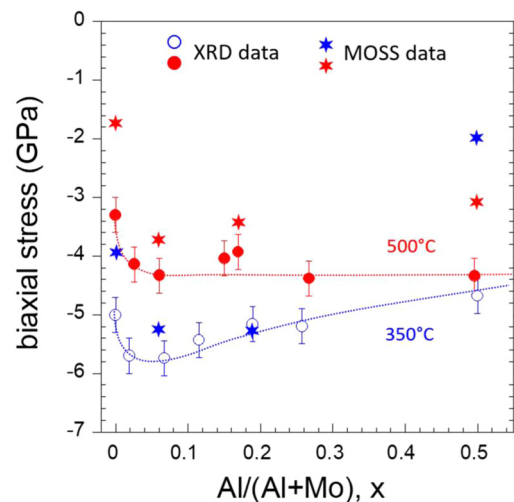
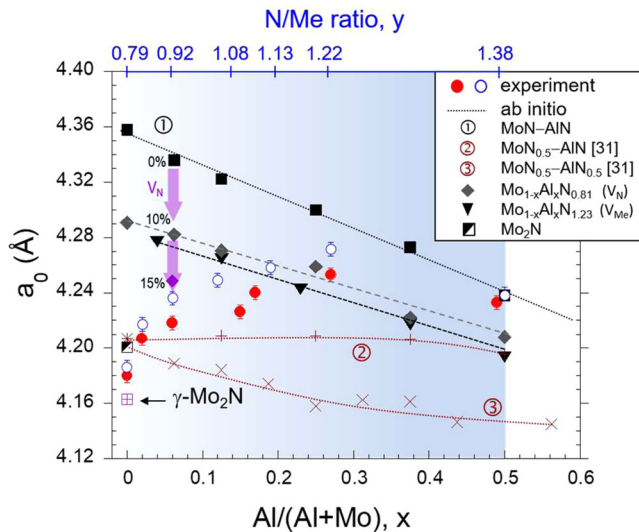


FIG. 6. Evolution of the in-plane stress of  $\text{Mo}_{1-x}\text{Al}_x\text{N}_y$  thin films with Al fraction,  $x$ , and substrate temperature  $T_s = 350^\circ\text{C}$  (blue open circles) and  $T_s = 500^\circ\text{C}$  (red filled circles). Circles correspond to residual stress values extracted from XRD strain-stress analysis, while stars refer to values of intrinsic stress obtained from *in situ* wafer curvature. Dotted lines are just a guide for the eye for the XRD stress values.



**FIG. 7.** Evolution of the stress-free lattice parameter,  $a_0$ , of  $\text{Mo}_{1-x}\text{Al}_x\text{N}_y$  thin films with Al fraction,  $x$ , and substrate temperature  $T_s = 350^\circ\text{C}$  (blue open circles) and  $T_s = 500^\circ\text{C}$  (red filled circles). The lattice constant of several ternary alloys with different vacancy concentrations obtained from DFT calculations (present work and from Ref. 31) is also reported. The purple vertical arrows illustrate the impact of  $V_N$  concentration on  $a_0$  for  $x = 0.06$ . The upper horizontal scale giving the N/Me ratio,  $y$ , in the films (with the corresponding variation also displayed as increasing hue of the blue shaded area) is only valid for the experiments.

film with  $x = 0.12$ , and then  $a_0$  tends to level off and eventually decreases to  $4.239 \pm 0.005 \text{ \AA}$  for  $x = 0.5$ , confirming the two distinct regimes of nitrogen incorporation as Al substitutes for Mo (see Fig. 1). A similar trend is revealed for the  $500^\circ\text{C}$  film series, albeit the values are found to be lower by a maximum of 0.4%, and nearly no change is observed at  $x = 0.5$ . The value of  $4.186 \text{ \AA}$  for our binary film is slightly above the bulk lattice parameter of the  $\gamma\text{-Mo}_2\text{N}$  compound ( $a_0 = 4.163 \text{ \AA}$ , according to JCPDS card No. 25-1366) due to the presence of more nitrogen but remains within the range of previously reported lattice constants for  $\gamma\text{-MoN}_x$  films.<sup>20–22,31</sup>

The stress evolution of  $\text{Mo}_{1-x}\text{Al}_x\text{N}_y$  films was also measured *in situ* during deposition using a wafer curvature. Figure 8 shows the MOSS data plotted as the stress thickness product  $\sigma_f \times h_f$  versus film thickness  $h_f$ . In this representation, the average stress  $\sigma_f$  at a given film thickness is simply obtained by dividing the quantity  $\sigma_f \times h_f$  by  $h_f$ , while the incremental stress is obtained from the derivative of the curve.<sup>42</sup> The values of  $\sigma_f$  for 300 nm thick films are reported in Fig. 6. All investigated films develop strongly compressive stress. The *in situ* MOSS data confirm the trends observed from XRD stress analysis, i.e., (1) larger compressive stresses are found for films deposited at lower substrate temperature and (2) more compressive stress is formed upon incorporating a few percent of Al ( $x = 0.06$ ) compared to the binary MoN film. They additionally reveal that for most samples a steady-state stress is reached (visualized as a constant slope in the plots of Fig. 8), except for the film with maximum Al content ( $x = 0.5$ ) deposited at  $T_s = 350^\circ\text{C}$ . For this latter case, the shape of the  $\sigma_f \times h_f$  versus  $h_f$

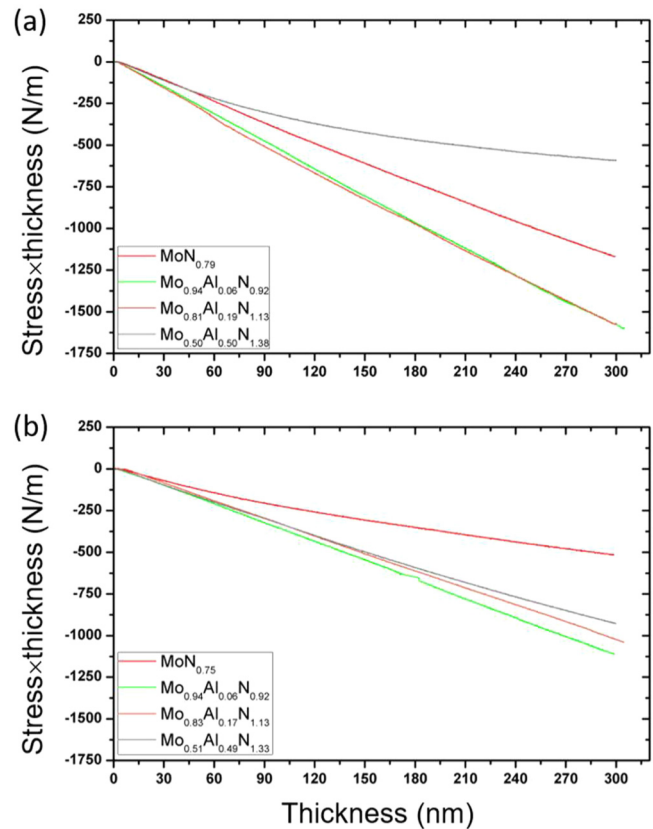


**FIG. 8.** *In situ* stress evolution, plotted as  $\sigma_f \times h_f$  vs  $h_f$ , during sputter-deposition of  $\text{Mo}_{1-x}\text{Al}_x\text{N}_y$  thin films at (a)  $350^\circ\text{C}$  and (b)  $500^\circ\text{C}$ , obtained using MOSS.

curve is typical of a film whose microstructure (grain size and/or texture) evolves with increasing film thickness, as often observed during competitive columnar growth of TiN films.<sup>63</sup> The presence of a mixed (111) + (001) texture (see Fig. 4) and development of more V-shaped columns [see Fig. 2(c)] support this scenario. Note that at  $T_s = 500^\circ\text{C}$ , this trend is not present any longer for the  $\text{Mo}_{0.51}\text{Al}_{0.49}\text{N}_{1.33}$  film for which a steady-state stress is observed. Despite the absolute stress values obtained from XRD and MOSS measurements are not directly comparable (only crystalline regions are probed by XRD and there is no thermal stress contribution to *in situ* MOSS data), they show similar trend with increasing Al fraction.

### C. Elastic and mechanical properties

The mechanical properties (indentation hardness and elastic modulus) of  $\text{Mo}_{1-x}\text{Al}_x\text{N}_y$  films were measured by nanoindentation tests. Figure 9 shows the evolution of hardness  $H$  with varying Al content. The variation is nonmonotonous, with  $H$  ranging from  $\sim 27$  to  $\sim 33$  GPa, and the maximum hardness  $H = 32.8 \pm 1.7$  GPa being achieved for the  $\text{Mo}_{0.81}\text{Al}_{0.19}\text{N}_{1.13}$  film deposited at  $350^\circ\text{C}$ .

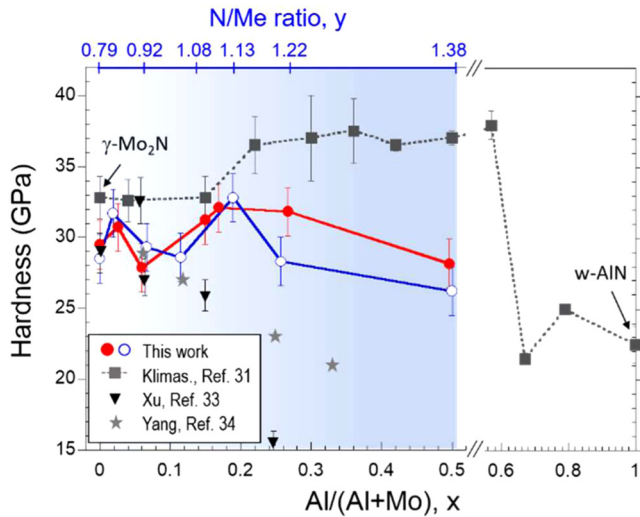


**FIG. 9.** Evolution of the hardness of  $\text{Mo}_{1-x}\text{Al}_x\text{N}_y$  thin films with Al fraction,  $x$ , and substrate temperature  $T_s = 350^\circ\text{C}$  (blue open circles) and  $T_s = 500^\circ\text{C}$  (red filled circles), obtained from nanoindentation tests. Values from previous works reported in the literature on sputter-deposited MoAlN films are also displayed for comparison purpose. The upper horizontal scale giving the N/Me ratio,  $y$ , in the films (with the corresponding variation also displayed as increasing hue of the blue shaded area) is only valid for the experiments.

No significant difference is observed between the two film series deposited at  $T_s = 350$  and  $500^\circ\text{C}$ . The binary  $\text{MoN}_{\sim 0.75}$  films exhibit a hardness of  $H \sim 29 \pm 1.5$  GPa, which is consistent with the value of  $\sim 30$  GPa reported by Klimashin *et al.*<sup>20</sup> for the  $\text{MoN}_{0.75}$  film. These values compare also well to those of 28.9<sup>33</sup> and 32.8 GPa<sup>31</sup> reported previously for sputtered  $\gamma\text{-MoN}_{0.5}$  films. These values are much higher than that of bulk MoN material ( $H = 17$  GPa).<sup>64</sup> The films with maximum Al content ( $x = 0.5$ ) have the lowest hardness of  $H = 27$  GPa. Our experimental  $H$  values for MoAlN alloys are in good agreement with those reported by Klimashin *et al.*<sup>31</sup> for  $x \leq 0.19$ . For  $0.19 < x \leq 0.5$ , our data evidence a decrease in hardness with an increase in the Al content, which was only observed at higher Al fraction ( $>0.57$ ) in the study by Klimashin *et al.*<sup>31</sup> (see Fig. 9), corresponding to the formation of wurtzite-type Al-rich MoAlN solid solutions.<sup>31</sup> In another study, however, Xu *et al.*<sup>33</sup> observed a continuous decrease in hardness from  $H = 32.6$  GPa ( $x = 0.06$ ) to  $H = 12.3$  GPa ( $x = 0.29$ ), but in their case, the nitrogen content was constant at  $\sim 36$  at.% and the MoAlN films had a (111) preferred orientation. A similar decreasing trend with the incorporation of Al was also observed by Yang *et al.*<sup>34</sup> in  $\text{Mo}_{1-x}\text{Al}_x\text{N}$  films with  $x$  rising up to 0.33. In that latter study, however, the nitrogen content was not quantified, which does not allow for a direct comparison.

The elastic modulus  $E_{IT}$  derived from nanoindentation shows also a complex dependence with Al content (see Fig. 10): starting from  $E = 300\text{--}320$  GPa for the binary films, the elastic modulus first decreases to 267 GPa for  $x = 0.06$  but then exhibits a peak at  $E = 320$  GPa for  $x = 0.15\text{--}0.19$ . A softening is then observed for

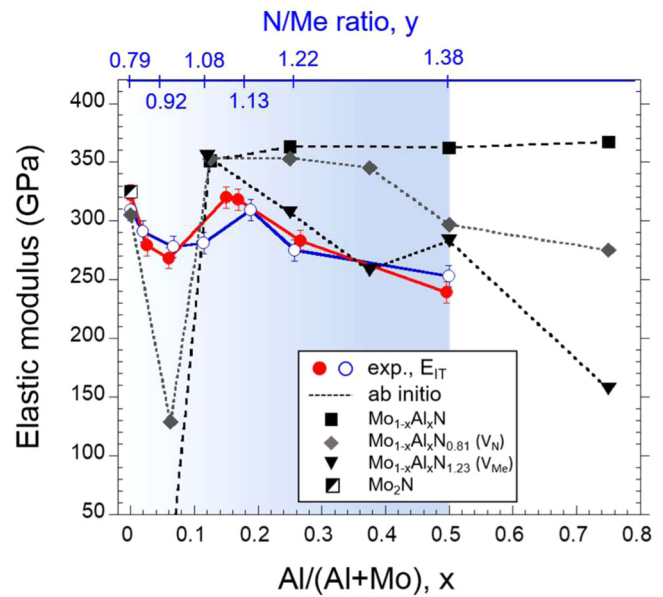


**FIG. 10.** Evolution of the elastic modulus ( $E_{IT}$ ) of  $\text{Mo}_{1-x}\text{Al}_x\text{N}_y$  thin films with Al fraction,  $x$ , and substrate temperature  $T_s = 350^\circ\text{C}$  (blue open circles) and  $T_s = 500^\circ\text{C}$  (red filled circles). Black symbols correspond to 0 K DFT values of Young's modulus  $E_{100}$  calculated along the  $\langle 100 \rangle$  direction for several ternary alloys with different vacancy concentrations. The upper horizontal scale giving the N/Me ratio,  $y$ , in the films (with the corresponding variation also displayed as increasing hue of the blue shaded area) is only valid for the experiments.

higher Al content, with values reaching  $E = 240$  GPa for  $x = 0.5$ . The same dependence is obtained for the  $500^\circ\text{C}$  film series, suggesting that these variations are intrinsically related to the film composition. Note that the elastic modulus values reported by Klimashin *et al.*<sup>31</sup> for sputter-deposited MoAlN films were in the 410–480 GPa range for Al fraction below  $x = 0.5$  and decreased down to 245 GPa for coatings containing wurtzite-type phases ( $x > 0.57$ ).

The transverse sound velocity,  $V_T$ , measured from BLS exhibits an almost linear increase from 3.66 to 5.57 km/s with the rise in Al fraction from  $x = 0$  to  $x = 0.5$  for the  $T_s = 350^\circ\text{C}$  film series [see Fig. 11(a)]. A similar evolution is also noticed for the  $T_s = 500^\circ\text{C}$  film series, albeit  $V_T$  values being systematically higher by 3%–5%. For  $x = 0$ , the value reported by Ozsdolay *et al.*<sup>65</sup> for the  $\text{MoN}_{0.75}$  epitaxial layer on MgO (001) is  $V_T = 3.32$  km/s, which is  $\sim 10\%$  lower than values for our binary  $\text{MoN}_{\sim 0.75}$  films. The evolution of shear elastic constant  $C_{44}$  with Al fraction is displayed in Fig. 11(b). Its variation exhibits first softening upon incorporation of a few percent of Al but then gradually increases with Al content from 122 GPa ( $x = 0.02$ ) to 136 GPa ( $x = 0.5$ ). A similar trend is found for the film series deposited at  $500^\circ\text{C}$ , the  $C_{44}$  values being systematically higher by 8–10 GPa. For  $\text{MoN}_{0.75}$  epitaxial layer, Ozsdolay *et al.*<sup>65</sup> measured a value of  $C_{44} = 86$  GPa, which is 37% lower than the value obtained for our binary  $\text{MoN}_{0.75}$  film ( $C_{44} = 136$  GPa). However, in their study, the layers were deposited

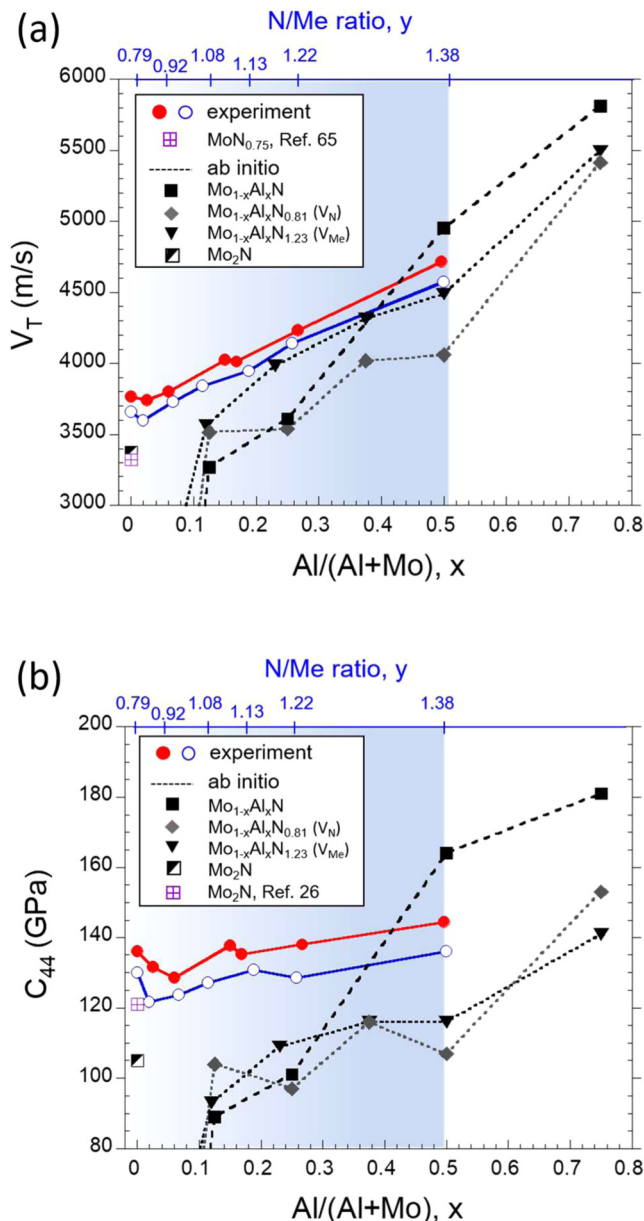


**FIG. 11.** Evolution of (a) the transverse sound velocity  $V_T$  and (b) the shear elastic constant  $C_{44}$  of  $\text{Mo}_{1-x}\text{Al}_x\text{N}_y$  thin films with Al fraction,  $x$ , and substrate temperature  $T_s = 350^\circ\text{C}$  (blue open circles) and  $T_s = 500^\circ\text{C}$  (red filled circles). Black symbols correspond to 0 K DFT calculations for several ternary alloys with different vacancy concentrations. The upper horizontal scale giving the N/Me ratio,  $y$ , in the films (with the corresponding variation also displayed as increasing hue of the blue shaded area) is only valid for the experiments.

at a much higher working pressure (2.67 Pa), resulting in under-dense layers (20% lower density compared to our films), which can explain their lower shear elastic constant, as well as a difference in the respective defects content.

## IV. DISCUSSION AND COMPARISON WITH AB INITIO CALCULATIONS

### A. Phase stability

The synthesis of  $\text{Mo}_{1-x}\text{Al}_x\text{N}_y$  thin films by reactive cosputter-deposition at constant  $\text{N}_2$  partial pressure has revealed the formation of ternary solid solutions with a cubic structure and a (001) preferred orientation, independently on the substrate temperature  $T_s = 350$  or  $500^\circ\text{C}$ . For  $x = 0$ , the XRD patterns evidence the stabilization of the  $\gamma$ - $\text{Mo}_2\text{N}$ -type phase (see Fig. 4) although the elemental composition of our binary MoN films indicates a higher nitrogen content,  $y \sim 0.75$ , compared to the  $\text{MoN}_{0.5}$  compound, suggesting a lower nitrogen vacancy concentration in our films and/or the presence of other types of defects (Mo vacancies, N antisites, or N interstitials). As our  $\text{MoN}_{\sim 0.75}$  films are very dense (see Fig. 3), the presence of metal vacancies would not be intuitively expected. However, the mass density derived from XRR is rather insensitive to the type of defects at the scale of the crystal lattice but instead to the overall averaged electronic density, as discussed in our previous work on TaN.<sup>60</sup> Prior works by Ozsdolay *et al.*<sup>22</sup> have shown that the cubic rock-salt  $\gamma$ - $\text{MoN}_x$  phase exists in a large range of N stoichiometry, from  $y = 0.69$  to  $y = 1.25$ , depending on the substrate temperature. Their study demonstrated that the  $\gamma$ - $\text{MoN}_x$  phase contains both metal and nitrogen vacancies: for instance, at  $T_s = 900^\circ\text{C}$ , they reported a stoichiometry of  $y = 0.75$  similar to ours, corresponding to a site occupancy of 60% and 80% for N and Mo atoms, respectively.

DFT calculations performed by Klimashin *et al.*<sup>20</sup> on a variety of  $\text{MoN}_y$  compounds show that the tetragonal  $\beta$ - $\text{MoN}_{0.5}$  phase (space group  $I4_1/amd$ ) with ordered nitrogen vacancies is most thermodynamically stable for  $y < 0.6$ , while the hexagonal  $\delta_2$ - $\text{MoN}_y$  (space group  $P6_3/mmc$ ) is the most stable for  $y > 0.75$ . The  $\gamma$ - $\text{MoN}_y$  phase with randomly distributed nitrogen vacancies is metastable, but its energy of formation exhibits a minimum for nitrogen compositions around  $y = 0.75$ , very close to our experimental value. Molybdenum nitrides also crystallize in a structure similar to  $\gamma$ - $\text{Mo}_2\text{N}$  with an excess of nitrogen in the lattice and with the formula  $\text{Mo}_3\text{N}_2$ .<sup>66</sup> Klimashin *et al.*<sup>20</sup> concluded that the evolution from  $\gamma$ - $\text{MoN}_{0.5}$  to  $\gamma$ - $\text{MoN}_{0.67}$  in their  $\text{MoN}_y$  films took place by filling vacancies at the N-sublattice rather than via the generation of vacancies at the Mo-sublattice.

Incorporation of Al into the cubic MoN lattice or the  $\gamma$ - $\text{Mo}_2\text{N}$  lattice is thermodynamically favorable, as first-principles calculations by Klimashin *et al.*<sup>31</sup> evidence a decrease of energy of formation  $E_F$  of  $\text{Mo}_{1-x}\text{Al}_x\text{N}_y$  solid solutions with increasing Al fraction. However, for fully occupied N sites, the rock-salt  $\text{Mo}_{1-x}\text{Al}_x\text{N}$  phase is metastable and the wurtzite  $\text{Mo}_{1-x}\text{Al}_x\text{N}$  phase is stabilized over the whole compositional range. Their DFT calculations also reveal an increasing solubility of Al in the cubic  $\text{Mo}_{1-x}\text{Al}_x\text{N}_y$  lattice with increasing N-vacancy content: the cubic phase is stable up to  $x = 0.45$  for  $\text{Mo}_{1-x}\text{Al}_x\text{N}_{0.5(1+x)}$  (actually corresponding to the  $\text{MoN}_{0.5}$ -AlN tie line) and up to  $x = 0.65$  for  $\text{Mo}_{1-x}\text{Al}_x\text{N}_{0.5}$  solid solutions. Our DFT calculations performed on several cubic  $\text{Mo}_{1-x}\text{Al}_x\text{N}_y$  phases confirm the decreasing  $E_F$  values with increasing  $x$  but also reveals that  $E_F$  critically depends on the type of defects ( $V_{\text{Me}}$ ,  $V_{\text{N}}$ ,  $N_{\text{Me}}$ , or interstitials) for a given  $x$  value, see Fig. S1 in the supplementary material.<sup>72</sup>  $E_F$  values are listed in

Table S1<sup>72</sup> in the supplementary material for all the investigated  $\text{Mo}_{1-x}\text{Al}_x\text{N}_y$  phases. While N interstitials and N antisites ( $N_{\text{Me}}$ ) are not thermodynamically favored,  $V_{\text{Me}}$  and  $V_{\text{N}}$  are thermodynamically favorable for  $x \leq 0.12$ , but then the defect-free  $\text{Mo}_{1-x}\text{Al}_x\text{N}$  phase becomes more stable at higher Al fraction. These results suggest that vacancies stabilize the cubic structure in ternary alloys with low Al content. Experimentally, the presence of N interstitials in the films cannot be completely ruled out as the bombardment of the growing layer with energetic particles (sputtered atoms and backscattered neutrals) would contribute to atomic displacement and creation of interstitials at the origin of film densification and compressive stress.<sup>42</sup>

## B. Chemical and structural properties

Based on the chemical analysis obtained from WDS, we have observed a significant nitrogen incorporation with increasing Al fraction in the films. If, overall, the increase corresponds to 1 N atom for 1 Al atom, the nonlinear evolution displayed in Fig. 1 points to a decreasing N incorporation rate at higher Al fraction. Two regimes could be identified, with a transition region around  $x = 0.12$ . Starting from  $\text{MoN}_{0.75}$ , the stoichiometry increases up to  $y \sim 1.35$  for the ternary film with the maximum Al content ( $x = 0.5$ ). This would suggest a progressive population of the octahedral nitrogen sites, followed by N incorporation into tetrahedral sites or a change in the site occupancy of Me vacancies, when Al substitutes for Mo. Our results on the compositional dependence  $y(x)$  differ from those reported by others.<sup>31,33</sup> These differences stem from different growth conditions in terms of power density, substrate temperature, deposition rate,  $\text{N}_2$  partial pressure, and elemental versus composite target, which are critical process parameters for reactive magnetron sputtering and stability of metastable phases triggered by kinetic effects rather than thermodynamic ones.<sup>67</sup>

The overall variation of  $\rho$  versus Al fraction is in agreement with the DFT calculations that predict a linear decrease in the mass density for defect-free, cubic  $\text{Mo}_{1-x}\text{Al}_x\text{N}$  alloys with increasing Al content, an indication of a correct evaluation of the average Al fraction from WDS. Obviously, the existence of N vacancies has little influence on mass density compared to Me ones, see computed values for cubic  $\text{Mo}_{1-x}\text{Al}_x\text{N}_{0.81}$  and  $\text{Mo}_{1-x}\text{Al}_x\text{N}_{1.23}$  alloys in Fig. 3. For low Al content  $x < 0.2$ , it can be noticed that the experimental mass density lies slightly above the calculated  $\rho$  values for defect-free  $\text{Mo}_{1-x}\text{Al}_x\text{N}$  alloys. This would support the existence of N vacancies (which slightly increase  $\rho$ ) rather than Me ones (which decrease  $\rho$ ) below  $x = 0.2$ . We can even infer from a comparison with the  $V_{\text{N}}$ -DFT line a concentration of  $V_{\text{N}}$  higher than 10% that should favor an even higher stiffening of the predicted Young's modulus below  $x = 0.1$  and a closer agreement to experiments, as one can see in Fig. 10. Above  $x = 0.25$ , the mass density follows closely the defect-free line. This would be consistent with the stabilization of less defective cubic  $\text{Mo}_{1-x}\text{Al}_x\text{N}_y$  phases with increasing  $x$ , as discussed in Sec. IV A.

The two regimes evidenced from the elemental composition analysis and XRR data also reflect in nonmonotonous evolution of the lattice parameter  $a_0$  versus Al fraction, as displayed in Fig. 7. Starting from  $a_0 \sim 4.183 \text{ \AA}$  for the binary  $\text{MoN}_{0.75}$  films (a value close to  $4.201 \text{ \AA}$  computed for  $\gamma\text{-MoN}_{0.5}$ ), the initial increase in  $a_0$

cannot be explained by Al incorporation only; one needs to consider a change in N vacancy concentration. Indeed, for  $x < 0.25$ , the lattice constant expansion with  $x$  is not reproduced by DFT either for the defect-free  $\text{Mo}_{1-x}\text{Al}_x\text{N}$  (curve ①) or for the  $\text{Mo}_{1-x}\text{Al}_x\text{N}_{0.5}$  (curve ③) alloys. The experimental values are closer to the  $a_0$  values computed for the  $\text{MoN}_{0.5}$ -AlN tie line (curve ②, corresponding to incorporation of 1 N for 2 Al), but the positive deviation would again suggest a higher N site occupancy rate at lower Al fraction, in accordance with the trends derived from Fig. 1. In the compositional range  $0.12 \leq x \leq 0.25$ , a good agreement is obtained with  $a_0$  values computed by DFT for cubic  $\text{Mo}_{1-x}\text{Al}_x\text{N}_{0.81}$  alloys, i.e., containing 10%  $V_{\text{N}}$  concentration. Above  $x = 0.25$ , an opposite trend is observed:  $a_0$  decreases with Al fraction, consistently with DFT calculations, and reaches curve ① for Al fraction around  $x = 0.5$ . As also illustrated in Fig. 7, the presence of nitrogen vacancies has tremendous effect on the lattice constant of  $\text{Mo}_{1-x}\text{Al}_x\text{N}_y$  alloys (see variations in  $a_0$  depicted by the vertical arrows for  $V_{\text{N}}$  concentrations up to 15%), while its impact on the mass density was marginal (see Fig. 3). This again supports the existence of  $V_{\text{N}}$  with concentration in the range of 15%–20% for films with  $x \leq 0.12$ , all the more that they are energetically favored (see Fig. S1).<sup>72</sup> This would correspond to a larger stiffening of the  $E_{100}$  Young's modulus (see Fig. 10) and  $C_{44}$  as well [see Fig. 12(b)].

Although the absolute elemental composition values for nitrogen derived from WDS can be questioned, the here observed  $a_0$  trend would suggest that the nonlinear N increase is qualitatively correct. One can also notice that  $a_0$  is slightly lower (between 0.2% and 0.4%) at higher substrate temperature (compare blue and red symbols in Fig. 7). This is an indication that the higher substrate temperature favors a slightly lower N concentration (due to desorption), as also reported by Ozsdolay *et al.* for  $\text{MoN}_y$  films.<sup>22,65</sup> It can be also anticipated that higher  $T_s$  would also favor defect annihilation, especially point defect of interstitial type created by energetic particle bombardment,<sup>42</sup> which would also contribute to  $a_0$  shrinkage.

## C. Elastic and mechanical properties

The similar evolutions of indentation hardness and elastic properties ( $E_{\text{IT}}$ ,  $V_{\text{T}}$ , and  $C_{44}$ ) with Al fraction for films deposited at  $T_s = 350 \text{ }^\circ\text{C}$  and  $500 \text{ }^\circ\text{C}$  displayed in Figs. 9–11 suggest that the mechanical and elastic properties of  $\text{Mo}_{1-x}\text{Al}_x\text{N}_y$  films are intrinsically related to the variation in film composition (both Al and N content, as discussed above) and are rather insensitive to atomic arrangement or microstructural attributes (grain size and stress state). We can suggest from the comparison of hardness values reported by Klimashin *et al.*<sup>31</sup> in Fig. 9 that higher hardness is retained upon Al+N incorporation when starting from an N vacancy concentration of 50%, i.e., close to  $\text{Mo}_2\text{N}$  for  $x = 0$ . In our case, the higher nitrogen content (or actually lower  $V_{\text{N}}$  concentration) at  $x = 0$  and the tendency to form  $V_{\text{Me}}$  at higher Al fraction would contribute to the slight decrease in hardness above  $x = 0.25$ . It is also interesting to note that the maximum hardness is achieved in the present study for  $\text{Mo}_{1-x}\text{Al}_x\text{N}_y$  films with nitrogen content close to stoichiometry ( $y = 1.13$ ). Figure 10 shows noteworthy that the influence of  $V_{\text{N}}$  below  $x = 0.1$  is prevailing on the huge stiffening of the  $E_{100}$  Young's modulus in comparison to

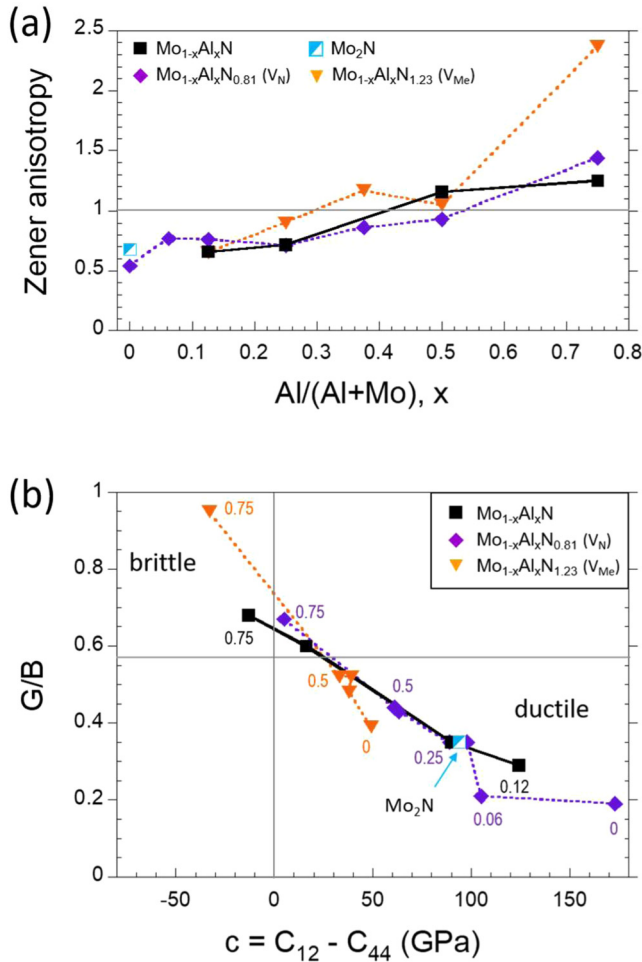


**FIG. 12.** Evolution of (a) elastic anisotropy (Zener factor  $A$ ) and (b)  $G/B$  vs Cauchy pressure  $c$  of cubic  $\text{Mo}_{1-x}\text{Al}_x\text{N}_y$  alloys with different Al content and vacancy concentration, as calculated by DFT. Numbers next to the symbols in (b) refer to Al fraction  $x$ .

the defect-free and  $V_{\text{Me}}$  cases, confirming the initial high  $V_{\text{N}}$  concentration above 10%.

In Fig. 11(a), the computed  $V_{\text{T}}$  of defect-free  $\text{Mo}_{1-x}\text{Al}_x\text{N}$  and defected  $\text{Mo}_{1-x}\text{Al}_x\text{N}_y$  exhibit merely the same continuous increasing trend as for experiments but lie much closer to experimental values above  $x \sim 0.25$  (for the  $V_{\text{Me}}$  case). The comparison between experimental and DFT  $V_{\text{T}}$  values again underlines two distinct regimes: the presence of mainly  $V_{\text{N}}$  vacancies below  $x \leq 0.12$  and in concentration much higher than 10%, and the tendency to form  $V_{\text{Me}}$  vacancies above 0.12. A mixture of  $V_{\text{N}}$  and  $V_{\text{Me}}$  with a high concentration of  $>10\%$  is also not excluded from the starting binary  $\text{MoN}_{0.75}$ , but with a larger effect of  $V_{\text{Me}}$  on the increment of  $V_{\text{T}}$  in comparison to the defect-free and  $V_{\text{N}}$  cases, in the 0.12–0.40 range. For  $x = 0.5$ , the experimental values  $V_{\text{T}} = 4.57$  km/s ( $T_{\text{s}} = 350$  °C) and 4.71 km/s ( $T_{\text{s}} = 500$  °C) lie between that of the

defect-free  $\text{Mo}_{0.5}\text{Al}_{0.5}\text{N}$  (4.94 km/s) and  $\text{Mo}_{0.5}\text{Al}_{0.5}\text{N}_{1.23}$  alloys containing 10%  $V_{\text{Me}}$  (4.50 km/s), suggesting a  $V_{\text{Me}}$  concentration lower than 10% at this stage. One can notice that increasing further the Al content above  $x = 0.5$  will lead to a similar influence of  $V_{\text{Me}}$  and  $V_{\text{N}}$  on  $V_{\text{T}}$  but not on the  $E_{100}$  Young's modulus.

The evolution of  $C_{44}$  versus Al fraction  $x$  is the result of two opposite trends between  $(V_{\text{T}})^2$  and  $\rho$  which increases and decreases with  $x$ , respectively, for the Mo-Al-N system. Here, we observe only a moderate continuous increase of  $C_{44}$  by  $\sim 10\%$ – $15\%$  for both experimental and predicted DFT values until  $x = 0.5$ . It is demonstrated from DFT simulations by Lahmer<sup>26</sup> that insertion of 3%  $V_{\text{Me}}$  and 6%  $V_{\text{N}}$  vacancies into  $\gamma$ - $\text{Mo}_2\text{N}$  leads to the reduction of all elastic constants, with a larger effect observed for  $V_{\text{Me}}$ . Here, when the ternary  $\text{Mo}_{1-x}\text{Al}_x\text{N}$  solid solution is formed, the influence of vacancy concentration (10%  $V_{\text{Me}}$  or  $V_{\text{N}}$  are considered here) on  $C_{44}$  is more complex and may change as a function of Al fraction. A complex dependence of the elastic properties of  $\text{V}_{1-x}\text{Al}_x\text{N}_y$  alloys to point defect and Al content was also reported recently by Rueß *et al.*<sup>68</sup> using DFT calculations.

Finally, let us examine the impact of the Al content and vacancy concentration on the elastic anisotropy and ductility of  $\text{Mo}_{1-x}\text{Al}_x\text{N}_y$  alloys, as predicted from DFT. Figure 12(a) plots the Zener anisotropy factor, defined as  $A = \frac{2C_{44}}{C_{11} - C_{12}}$ , as a function of Al fraction for several defect-free and defected alloys. The anisotropy factor increases from  $A \sim 0.5$  at  $x = 0$  to  $A \sim 2.3$  at  $x = 0.75$ . The impact of  $V_{\text{N}}$  or  $V_{\text{Me}}$  does not affect much of the  $A$  values up to  $x = 0.5$ , albeit that the presence of metal vacancies tends to increase the elastic anisotropy (this is particularly visible at  $x = 0.75$ ). A greater elastic anisotropy was also reported in  $\text{Ti}_{1-x}\text{Al}_x\text{N}$  alloys with increasing Al content and ascribed to more directional covalent bonding.<sup>69</sup> For the Mo-Al-N system, an isotropic elastic behavior ( $A \sim 1$ ) is predicted for  $\text{Mo}_{1-x}\text{Al}_x\text{N}_y$  alloys with  $0.4 \leq x \leq 0.5$ . This compositional range is close to what has been calculated for the Ti-Al-N system for which  $A = 1$  at  $x = 0.28$ .<sup>69</sup>

On the other hand, the type of defects is found to more significantly alter the ductile character of  $\text{Mo}_{1-x}\text{Al}_x\text{N}_y$  alloys, as shown in Fig. 12(b). This graph plots the evolution of the shear modulus to bulk modulus ratio,  $G/B$ , as a function of the Cauchy pressure  $c = C_{12} - C_{44}$ . This representation is based on Pugh<sup>70</sup> and Pettifor<sup>71</sup> criteria and allows to identify the region of brittleness ( $G/B > 0.57$  and  $c < 0$ ) and ductility ( $G/B \leq 0.57$  and  $c > 0$ ).<sup>47</sup> As stated in the Introduction,  $\text{MoN}_y$  compounds are quite ductile materials, and this is confirmed by the present DFT calculations on  $\text{MoN}_{0.5}$  and  $\text{MoN}_{0.81}$ . Interestingly, Fig. 12(b) reveals that (1) the incorporation of Al even up to  $x = 0.5$  does not compromise much on ductility and (2) the presence of N vacancies is found to be more beneficial in retaining the ductile properties of Mo-Al-N compared to Me ones. This can be explained by a greater metallic bonding character (positive Cauchy pressure) for the  $V_{\text{N}}$  case.

## V. CONCLUSIONS

To conclude, by employing *ab initio* calculations and thin film growth experiments, we have systematically studied the influence of the Al content and the nitrogen-to-metal ratio on the structure and elastic properties of the Mo-Al-N system. It is shown that point

defects, especially nitrogen vacancies below  $x=0.12$  and metal vacancies above the value, play a key role in the compositional dependence of the lattice constant, Young modulus  $E_{100}$ , and shear elastic constant  $C_{44}$  of this system, which in part explains the extensive spread of elastic moduli reported in the literature, ranging from 223 to 450 GPa.

Experimentally,  $\text{Mo}_{1-x}\text{Al}_x\text{N}_y$  solid solution thin films are formed in the cubic rock-salt structure, with the (001) preferred orientation, in the whole compositional range investigated ( $0 \leq x \leq 0.5$ ) by using reactive magnetron cosputtering at fixed  $P_{\text{N}_2}$  and changing the power density applied to the elemental Mo and Al targets. The variation in the substrate temperature from 350 to 500 °C has little influence on the structural and elastic properties of the  $\text{Mo}_{1-x}\text{Al}_x\text{N}_y$  films. A salient feature of the present work is that the incorporation of Al into MoN is accompanied by a significant variation in the nitrogen content from 44% ( $x=0$ ) to 58% ( $x=0.5$ ), despite a constant  $\text{N}_2$  partial pressure during deposition. In particular, the incorporation rate of N is not monotonous, being much stronger at low Al fraction  $x \leq 0.12$ .

It is evidenced that ternary  $\text{Mo}_{1-x}\text{Al}_x\text{N}_y$  alloys with low Al content ( $x=0.02-0.12$ ) tend to stabilize primarily nitrogen vacancies in the concentration between 10% and 20%, while the incorporation of a higher Al fraction (up to  $x=0.5$ ) results in the formation of less defective films. DFT calculations confirm that the existence of nitrogen vacancies in cubic  $\text{Mo}_{1-x}\text{Al}_x\text{N}_y$  solid solutions is energetically favorable for  $x \leq 0.12$  and contributes as well to the mechanical stability of the cubic structure by a huge stiffening of  $E_{100}$  and  $C_{44}$ . For  $x > 0.12$ , the comparison of experimental Young modulus and shear modulus to DFT calculations advocates in favor of the stabilization of metal vacancies (less than 10%).

The maximum hardness is obtained for the  $\text{Mo}_{0.81}\text{Al}_{0.19}\text{N}_{1.13}$  film for which the N/Me ratio is close to stoichiometry, with a corresponding elastic modulus of  $\sim 300$  GPa. Films with larger Al content ( $x=0.25$  and  $x=0.5$ ) exhibit worse mechanical properties (H 27 GPa and elastic modulus  $\sim 245$  GPa), which could be explained by more covalent bonding. DFT calculations predict that the ductile character of ternary Mo-Al-N alloys can be retained in a large compositional range up to  $x=0.5$ . Overall, the knowledge gained from this combined experimental and modelling work underlines the importance of point defects in the stabilization and elastic properties of metastable MoN-based cubic systems, similarly to what has been reported for other TMNs involving group 5 (Ta) or group 6 (W) metals. Furthermore, these findings may be relevant to further optimize the structure and strength of other Me-Al-N coatings by appropriate tuning of elemental composition and point-defect engineering concept.

## ACKNOWLEDGMENTS

F.A. acknowledges the Scientific and Technical Research Council of Turkey (TÜBİTAK) for fellowship granted in the frame of 2219-International Post-Doctoral Research Fellowship (Contract No. 1059B191800197). L.L. and D.H. gratefully acknowledge financial support from the Austrian Science Fund (FWF) under Project No. P30341-N36. The computational results presented have been achieved using the Vienna Scientific Cluster (VSC).

## REFERENCES

- <sup>1</sup>J. E. Sundgren, *Thin Solid Films* **128**, 21 (1985).
- <sup>2</sup>P. Patsalas, N. Kalfagiannis, and S. Kassavetis, *Materials* **8**, 3128 (2015).
- <sup>3</sup>P. Patsalas, N. Kalfagiannis, S. Kassavetis, G. Abadias, D. V. Bellas, C. Lekka, and E. Lidorikis, *Mater. Sci. Eng. R Rep.* **123**, 1 (2018).
- <sup>4</sup>U. Guler, J. C. Ndukaife, G. V. Naik, A. G. A. Nnanna, A. V. Kildishev, V. M. Shalaev, and A. Boltasseva, *Nano Lett.* **13**, 6078 (2013).
- <sup>5</sup>A. Lalis, G. Tessier, J. Plain, and G. Baffou, *Sci. Rep.* **6**, 38647 (2016).
- <sup>6</sup>H. Lind, F. Tasnádi, and I. A. Abrikosov, *New J. Phys.* **15**, 95010 (2013).
- <sup>7</sup>I. A. Saladukhin, G. Abadias, V. V. Uglov, S. V. Zlotski, A. Michel, and A. Janse van Vuuren, *Surf. Coatings Technol.* **332**, 428 (2017).
- <sup>8</sup>D. G. Sangiovanni, V. Chirita, and L. Hultman, *Phys. Rev. B* **81**, 104107 (2010).
- <sup>9</sup>H. Kindlund *et al.*, *APL Mater.* **1**, 42104 (2013).
- <sup>10</sup>K. Balasubramanian, S. V. Khare, and D. Gall, *Acta Mater.* **152**, 175 (2018).
- <sup>11</sup>H. Kindlund, D. G. Sangiovanni, I. Petrov, J. E. Greene, and L. Hultman, *Thin Solid Films* **688**, 137479 (2019).
- <sup>12</sup>J. Chen, L. L. Boyer, H. Krakauer, and M. J. Mehl, *Phys. Rev. B* **37**, 3295 (1988).
- <sup>13</sup>M. B. Kanoun, S. Goumri-Said, and M. Jaouen, *Phys. Rev. B* **76**, 134109 (2007).
- <sup>14</sup>Y. Linghu, X. Wu, R. Wang, W. Li, and Q. Liu, *J. Electron Mater.* **46**, 1914 (2017).
- <sup>15</sup>N. Koutná, R. Hahn, J. Zálešák, M. Friák, M. Bartosik, J. Keckes, M. Šob, P. H. Mayrhofer, and D. Holec, *Mater. Des.* **186**, 108211 (2020).
- <sup>16</sup>H. Kindlund, D. G. Sangiovanni, J. Lu, J. Jensen, V. Chirita, J. Birch, I. Petrov, J. E. Greene, and L. Hultman, *Acta Mater.* **77**, 394 (2014).
- <sup>17</sup>D. G. Sangiovanni, *Acta Mater.* **151**, 11 (2018).
- <sup>18</sup>H. Jehn and P. Ettmayer, *J. Less-Common Met.* **58**, 85 (1978).
- <sup>19</sup>I. Jauberteau, A. Bessaudou, R. Mayet, J. Cornette, J. L. Jauberteau, P. Carles, and T. Merle-Méjean, *Coatings* **5**, 656 (2015).
- <sup>20</sup>F. F. Klimashin, N. Koutná, H. Euchner, D. Holec, P. H. Mayrhofer, N. Koutná, H. Euchner, D. Holec, and P. H. Mayrhofer, *J. Appl. Phys.* **120**, 185301 (2016).
- <sup>21</sup>N. Koutná, D. Holec, O. Svoboda, F. F. Klimashin, and P. H. Mayrhofer, *J. Phys. D Appl. Phys.* **49**, 375303 (2016).
- <sup>22</sup>B. D. Ozsdolay, K. Balasubramanian, and D. Gall, *J. Alloys Compd.* **705**, 631 (2017).
- <sup>23</sup>K. Balasubramanian, L. Huang, and D. Gall, *J. Appl. Phys.* **122**, 195101 (2017).
- <sup>24</sup>K. Balasubramanian, S. V. Khare, and D. Gall, *Acta Mater.* **159**, 77 (2018).
- <sup>25</sup>B. Bouaouina, A. Besnard, S. E. Abaidia, A. Airoudj, and F. Bensouici, *Surf. Coatings Technol.* **333**, 32 (2018).
- <sup>26</sup>M. A. Lahmer, *Comput. Condens. Matter* **21**, e00405 (2019).
- <sup>27</sup>S. Kassavetis *et al.*, *J. Phys. Chem. C* **123**, 21120 (2019).
- <sup>28</sup>G. Gassner, P. H. Mayrhofer, K. Kutschej, C. Mitterer, and M. Kathrein, *Surf. Coatings Technol.* **201**, 3335 (2006).
- <sup>29</sup>S. A. Glatz, C. M. Koller, H. Bolvardi, S. Kolozsvári, H. Riedl, and P. H. Mayrhofer, *Surf. Coatings Technol.* **311**, 330 (2017).
- <sup>30</sup>J. C. Schuster and H. Nowotny, *J. Mater. Sci.* **20**, 2787 (1985).
- <sup>31</sup>F. F. Klimashin, H. Euchner, and P. H. Mayrhofer, *Acta Mater.* **107**, 273 (2016).
- <sup>32</sup>J. Ština, J. Musil, and P. Dohnal, *Vacuum* **80**, 588 (2006).
- <sup>33</sup>J. Xu, H. Ju, and L. Yu, *Vacuum* **103**, 21 (2014).
- <sup>34</sup>J. F. Yang, Z. G. Yuan, Q. Liu, X. P. Wang, and Q. F. Fang, *Mater. Res. Bull.* **44**, 86 (2009).
- <sup>35</sup>J. J. Colin, Y. Diot, P. Guerin, B. Lamongie, F. Berneau, A. Michel, C. Jaouen, and G. Abadias, *Rev. Sci. Instrum.* **87**, 23902 (2016).
- <sup>36</sup>L. G. Parratt, *Phys. Rev.* **95**, 359 (1954).
- <sup>37</sup>T. H. de Keijser, J. I. Langford, E. J. Mittemeijer, and A. B. P. Vogels, *J. Appl. Crystallogr.* **15**, 308 (1982).
- <sup>38</sup>I. C. Noyan and J. B. Cohen, *Residual Stress Measurement by Diffraction and Interpretation* (Springer-Verlag, New York, 1987).

- <sup>39</sup>U. Welzel, J. Ligot, P. Lamparter, A. C. Vermeulen, and E. J. Mittemeijer, *J. Appl. Crystallogr.* **38**, 1 (2005).
- <sup>40</sup>G. Abadias, *Surf. Coatings Technol.* **202**, 2223 (2008).
- <sup>41</sup>J. A. Floro, E. Chason, and S. R. Lee, *Mater. Res. Soc. Symp. Proc.* **406**, 491 (1996).
- <sup>42</sup>G. Abadias *et al.*, *J. Vac. Sci. Technol. A* **36**, 20801 (2018).
- <sup>43</sup>A. Fillon, G. Abadias, A. Michel, and C. Jaouen, *Thin Solid Films* **519**, 1655 (2010).
- <sup>44</sup>G. G. Stoney, *Proc. R. Soc. London* **82**, 172 (1909).
- <sup>45</sup>G. C. A. M. Janssen, M. M. Abdalla, F. van Keulen, B. R. Pujada, and B. van Venrooy, *Thin Solid Films* **517**, 1858 (2009).
- <sup>46</sup>P. Djemia, F. Ganot, P. Moch, V. Branger, and P. Goudeau, *J. Appl. Phys.* **90**, 756 (2001).
- <sup>47</sup>G. Abadias, P. Djemia, and L. Belliard, *Surf. Coatings Technol.* **257**, 129 (2014).
- <sup>48</sup>G. Carlotti, *Appl. Sci.* **8**, 124 (2018).
- <sup>49</sup>A. Kueny and M. Grimsditch, *Phys. Rev. B* **26**, 4699 (1982).
- <sup>50</sup>F. Nizzoli and J. R. Sandercock, in *Dynamical Properties of Solids*, edited by G. K. Horton and A. A. Maradudin (North Holland, Amsterdam, 1990), pp. 281–335.
- <sup>51</sup>W. C. Oliver and G. M. Pharr, *J. Mater. Res.* **19**, 3 (2004).
- <sup>52</sup>G. Kresse, *Phys. Rev. B* **59**, 1758 (1999).
- <sup>53</sup>G. Kresse and J. Furthmüller, *Phys. Rev. B* **54**, 11169 (1996).
- <sup>54</sup>S.-H. Wei, L. G. Ferreira, J. E. Bernard, and A. Zunger, *Phys. Rev. B* **42**, 9622 (1990).
- <sup>55</sup>R. Yu, J. Zhu, and H. Q. Ye, *Comput. Phys. Commun.* **181**, 671 (2010).
- <sup>56</sup>M. Moakher and A. N. Norris, *J. Elast.* **85**, 215 (2006).
- <sup>57</sup>H. Titrian, U. Aydin, M. Friák, D. Ma, D. Raabe, and J. Neugebauer, *MRS Proc.* **1524**, Mrsf12 (2013).
- <sup>58</sup>M. Friák, W. A. Counts, D. Ma, B. Sander, D. Holec, D. Raabe, and J. Neugebauer, *Materials* **5**, 1853 (2012).
- <sup>59</sup>G. Abadias, L. E. Koutsokeras, A. Siozios, and P. Patsalas, *Thin Solid Films* **538**, 56 (2013).
- <sup>60</sup>G. Abadias, C.-H. Li, L. Belliard, Q. M. Hu, N. Greneche, and P. Djemia, *Acta Mater.* **184**, 254 (2020).
- <sup>61</sup>M. Maoujoud, M. Jardinier-Offergeld, and F. Bouillon, *Appl. Surf. Sci.* **64**, 81 (1993).
- <sup>62</sup>G. Abadias, L. E. Koutsokeras, S. N. Dub, G. N. Tolmachova, A. Debelle, T. Sauvage, and P. Villechaise, *J. Vac. Sci. Technol. A* **28**, 541 (2010).
- <sup>63</sup>G. Abadias and P. Guerin, *Appl. Phys. Lett.* **93**, 111908 (2008).
- <sup>64</sup>L. E. Toth, *Transition Metal Carbides and Nitrides* (Academic, New York, 1971).
- <sup>65</sup>B. D. Ozsdolay, X. Shen, K. Balasubramanian, G. Scannell, L. Huang, M. Yamaguchi, and D. Gall, *Surf. Coatings Technol.* **325**, 572 (2017).
- <sup>66</sup>N. V. Troitskaya and Z. G. Pinsker, *Sov. Phys. Crystallogr.* **4**, 33 (1960).
- <sup>67</sup>S. Liu, K. Chang, S. Mráz, X. Chen, M. Hans, D. Music, D. Primetzhofer, and J. M. Schneider, *Acta Mater.* **165**, 615 (2019).
- <sup>68</sup>H. Rueß, D. Music, A. Bahr, and J. M. Schneider, *J. Phys. Condens. Matter* **32**, 25901 (2020).
- <sup>69</sup>F. Tasnádi, I. A. Abrikosov, L. Rogström, J. Almer, M. P. Johansson, and M. Od'án, *Appl. Phys. Lett.* **97**, 2010 (2010).
- <sup>70</sup>S. F. Pugh, *Philos. Mag.* **45**, 823 (1954).
- <sup>71</sup>D. G. Pettifor, *Mater. Sci. Technol.* **8**, 345 (1992).
- <sup>72</sup>See supplementary material at <https://doi.org/10.1116/6.0000292> for computed DFT values of formation energies, structural, and elastic properties of Mo<sub>1-x</sub>Al<sub>x</sub>Ny alloys.